Full Title: Ablation of parasympathetic cholinergic innervation of the liver prevents diet-induced obesity and hepatic steatosis in mice.

Authors

Jiyeon Hwang[1,2], Junichi Okada[1,2], Li Liu[1,2], Jeffrey E. Pessin[1,2,3], Gary J. Schwartz[1,2], and Young-Hwan Jo[1,2,3]*

Affiliations

[1]The Fleischer Institute for Diabetes and Metabolism

[2]Division of Endocrinology, Department of Medicine

[3]Department of Molecular Pharmacology, Albert Einstein College of Medicine, NY, USA

*** Corresponding author: young-hwan.jo@einsteinmed.edu**

Departments of Medicine and Molecular Pharmacology

Albert Einstein College of Medicine,

1300 Morris Park Ave, Bronx, NY 10461

Tel: 718-430-3495

Abstract

The role of parasympathetic cholinergic innervation in hepatic lipid metabolism has been the subject of considerable debate because of a lack of neuroanatomical studies. We investigate the impact of the loss of function of parasympathetic cholinergic innervation to the liver on hepatic lipid metabolism in mice fed a high-fat diet (HFD). Our results, obtained through immunostaining and 3D imaging of cleared liver tissue, reveal the presence of muscarinic acetylcholine receptors and parasympathetic nerve originating from the dorsal motor nucleus of the vagus in hepatocytes. Deleting this innervation reduces body weight and increases energy expenditure. Ablating these neurons prevents hepatic steatosis and leads to browning of inguinal white adipose tissue. Loss of hepatic cholinergic input increases hepatic *Cyp7b1* expression and serum bile acid levels. Knockdown of the G protein-coupled bile acid receptor 1 gene in inguinal white adipose tissue reverses the beneficial effects of the loss of hepatic cholinergic function on hepatic steatosis. These findings suggest that modulating the parasympathetic cholinergic innervation of the liver may offer a therapeutic avenue for restoring lipid metabolism in obesity and diabetes.

Teaser

The parasympathetic nervous system of the liver regulates the secretion of bile acids and the development of hepatic steatosis.

Introduction

The liver plays a major role in controlling energy metabolism, including macronutrient metabolism, lipid homeostasis, and energy storage (*1*). Like other visceral organs (*2-4*), the liver is innervated by the vagus nerve (*5*), and vagal innervation to the liver regulates these metabolic functions (*6-9*). Parasympathetic (or vagal) efferent neurons innervating the liver are located in the dorsal motor nucleus of the vagus (DMV) (*10*). Prior anatomical studies with retrograde neuronal tracers such as cholera toxin B, pseudorabies virus, and AAV encoding a Cre-inducible reporter protein demonstrate that the mouse liver receives parasympathetic nerve innervation from the DMV (*11-13*). DMV motor neurons are acetylcholine (ACh)-expressing neurons (*2*). We recently showed that hepatocytes receive direct DMV cholinergic input and express muscarinic ACh receptor genes (mAChRs) (*12*). Importantly, a short-term change in the activity of DMV cholinergic neurons projecting to the liver regulates the hepatic glucose output in lean mice (*12*). In contrast to these prior findings, recent 3D imaging studies have revealed a paucity of parasympathetic cholinergic innervation in the mouse liver (*14, 15*), indicating that hepatic metabolism is primarily regulated by the sympathetic nervous system. Therefore, it is essential to re-examine the cholinergic system in the liver to gain a better understanding of how the autonomic nervous system of the liver controls metabolic homeostasis.

Nonalcoholic fatty liver disease (NAFLD) is characterized by the accumulation of excessive amounts of fat in the liver, which is determined by multiple factors including the uptake of fatty acids by hepatocytes, *de novo* lipogenesis (DNL), mitochondrial and peroxisomal fatty acid oxidation, and lipid export from the liver (*16, 17*). These pathways are downstream targets of the autonomic nervous system. A recent study reveals that significant alterations in sympathetic innervation to the liver, such as swollen axonal varicosities, nerve fiber retraction, and abnormal axonal sprouting, are associated with NAFLD in mice and humans (*15*), supporting the critical role of sympathetic nerve plasticity in hepatic lipid metabolism. However, it has been demonstrated that the vagus nerve exerts a significant influence on the regulation of hepatic lipid metabolism. For example, activation of central leptin receptors reduces hepatic fat accumulation, which requires hepatic vagal innervation in lean and high-fat fed rodents (*7*). Similarly, the anti-steatotic effect of leptin is dependent on vagal innervation in humans (*18*). In addition, central infusion of oleic acid suppresses triglyceride-rich very low-density lipoproteins (VLDL-TG) secretion through hepatic vagal innervation in rats (*19*). The hepatic vagus nerve regulates the development of NAFLD via altering hepatic inflammation (*9*). However, there is a serious caveat in the vagal nerve denervation experiments. Given the fact that both vagal sensory and parasympathetic cholinergic fibers traverse through the hepatic vagus nerve, hepatic vagal denervation cuts both, making interpretation of the results difficult. Hence, the role of the parasympathetic cholinergic innervation of the liver in controlling hepatic lipid metabolism remains to be elucidated.

Dynamic crosstalk between the liver and white adipose tissue (WAT) appears essential for hepatic fat accumulation and the development of NAFLD (*20*). VLDL-TG synthesized in the liver is secreted and transported to adipose tissue for storage in the postprandial state (*1*). Fasting increases lipolysis in adipocytes, and the free fatty acids released from WAT are transported to the liver for energy metabolism (*1*). In a human study, most fatty acids constituting VLDL-TG are derived from adipose tissue (*21*). However, in obesity, adipose tissue can no longer effectively store lipids, thus redirecting them toward other organs, primarily the liver (*20*). Increased lipolysis, along with elevated cytokine release from WAT, causes hepatic steatosis (*20*). Interestingly, the liver has the capability to control lipid uptake and lipolysis in WAT by activating bile acid (BA) signaling pathways (*22*). Vagotomized rats exhibit reduced expression of the cholesterol 7 alpha-hydroxylase (*Cyp7a1*) gene, the rate-limiting enzyme in the classic bile acid synthesis pathway in the liver, while displaying increased bile acid levels in the serum and bile, in part via enhanced intestinal passive absorption of BAs (*23*). Biliary epithelial cells in rats express the muscarinic acetylcholine receptor type 1 and its activation by carbachol reduces bile flow (*24*). The parasympathetic cholinergic innervation to the liver may potentially exert a regulatory effect on bile acid synthesis and outflow from the liver, which could subsequently result in a decrease in lipolysis within the white adipose tissue.

In this study, we analyzed the effects of eliminating cholinergic neurons projecting to the liver on lipid metabolism in mice fed a high-fat diet. Our examination used 2D immunostaining and 3D imaging of cleared liver tissue, which revealed that hepatocytes received direct input from the DMV and expressed muscarinic acetylcholine receptors. The ablation of parasympathetic cholinergic neurons innervating the liver prevented hepatic steatosis in mice fed a high-fat diet. This reduced fat accumulation in the liver was associated with bile acid-induced beiging of ingWAT through activation of the G protein-coupled bile acid receptor 1 (GPBAR1 or TGR5) in ingWAT.

Results

Parasympathetic cholinergic innervation of the liver

In our previous study (*12*), we showed that a subset of DMV cholinergic neurons projected to the liver. To extend and further confirm the presence of DMV cholinergic neurons innervating the liver, we injected a Cre-dependent viral tracer (adeno-associated virus (AAV).PHP.eB-FLEX-tdTomato (*25*)) into the liver of choline acetyltransferase (ChAT)-IRES-Cre ($ChAT^{Cre}$) mice (*26*). The $ChAT^{Cre}$ transgenic strain has been used to selectively label parasympathetic cholinergic neurons (*27*). At 3 weeks post-viral infection, we performed double immunocytochemistry with anti-ChAT and anti-tdTomato antibodies on the brain sections and found that the DMV displayed a small number of tdTomato-positive cells (Fig. 1A). Importantly, all tdTomato-positive cells in the DMV were ChAT-expressing cells (n = 72 out of 72 neurons from 3 mice), and approximately 10 % of DMV cholinergic neurons expressed tdTomato (range, 7–14 %; n= 72 out of 660 cholinergic neurons from 3 mice). We also injected retrograde AAV-FLEX-eGFP into the livers of the $ChAT^{Cre}$ mice. Three weeks later, the brain tissue was collected, cleared, and stained with anti-ChAT and anti-GFP antibodies. Likewise, a subset of DMV cholinergic neurons were labeled with an anti-GFP antibody. Hence, our results are consistent with prior findings that a subset of DMV cholinergic neurons innervate the liver (*11-13*).

We investigated whether the liver receives cholinergic innervation by immunostaining with an antibody against the presynaptic cholinergic marker vesicular acetylcholine transporter (vAChT). Our analysis revealed the presence of vAChT-positive nerve terminal puncta scattered throughout the liver parenchyma, including in the periportal, midlobular, and pericentral zones (Fig. 1B). As recent 3D imaging studies of cleared liver tissue have shown a paucity of cholinergic innervation, we cleared mouse liver tissues (Fig. 1C), and stained for vAChT. Our 3D imaging analysis of the cleared liver tissue clearly showed numerous vAChT-positive nerve terminals in the liver parenchyma (Fig. 1C) . We then evaluated the origin of these cholinergic nerve terminals. We injected an anterograde AAV1 encoding a Cre-inducible tdTomato and a synaptophysin-GFP (sypGFP) fusion protein separated by the sequence of a T2A self-cleaving peptide (AAV1-FLEX-tdTomato-T2A-sypGFP (*28*)) into the DMV of $ChAT^{Cre}$ mice. Under these experimental conditions, we anticipated that tdTomato would be expressed in DMV cholinergic neurons, and that sypGFP would move forward to the axon terminals of DMV cholinergic neurons. As shown in Fig. 1D, immunostaining revealed that the DMV cholinergic neurons were positive for tdTomato, indicating that the DMV cholinergic neurons were successfully infected. Immunolabeling of liver sections further revealed numerous sypGFP-positive puncta in hepatocytes and bile duct epithelial cells cholangiocytes (Fig. 1D). Interestingly, the individual cholangiocytes were surrounded by sypGFP-positive puncta and vAChT-positive nerve terminals (Fig. 1D and Fig. S1A).

In addition, 3D imaging of cleared liver tissue collected from ChAT^{Cre} mice injected with AAV1-FLEX-tdTomato-T2A-sypGFP indicated cholinergic nerve terminals around the portal vein and throughout the liver parenchyma (Fig. 1E) . These GFP-positive nerve terminals were also stained for the vAChT (Fig. 1F) . In addition to cholinergic input, Western blot analysis of liver tissue homogenates revealed the presence of muscarinic ACh receptor types 1, 2, 4, and 5 (CHRM1, 2, 4, and 5), but not CHRM3 (Fig. 1G). As CHRM4 was highly expressed compared to other CHRM subtypes, we immunolabeled the liver tissues with an anti-CHRM4 antibody. CHRM4 was detected in areas adjacent to vAChT-positive terminals (Fig. 1H). Similarly, CHRM2 was also found in hepatocytes (Fig. S1B). Taken together, our 3D imaging of cleared tissues in conjunction with anterograde neural tracing and immunostaining provides compelling evidence that the liver is a downstream target of the parasympathetic cholinergic neurons.

Loss of parasympathetic cholinergic neurons innervating the liver reduces body weight during high-fat diet feeding.

The role of DMV cholinergic neurons innervating the liver in controlling metabolic homeostasis remains unexplored. We examined the physiological impact of hepatic cholinergic loss-of-function on energy homeostasis. For these experiments, we used a retrograde AAV (AAVrg) encoding a Cre-inducible diphtheria toxin subunit A fragment (dtA) that induces apoptosis of target cells (*29*). AAVrg-FLEX-dtA and AAVrg-FLEX-GFP as control were injected into the livers of the ChAT^{Cre} mice (Fig. 2A). To validate cholinergic cell death in the DMV, we sacrificed mice at 10 weeks post-viral inoculation and stained the DMV cholinergic neurons with an anti-ChAT antibody. The number of DMV cholinergic neurons was significantly lower in ChAT^{Cre} mice that received retroAAV-FLEX-dtA than in the controls (Fig. 2B, C and Fig. S4). This reduced number of DMV cholinergic neurons was strongly associated with a lack of vAChT-positive nerve terminals in the livers of ChAT^{Cre} mice that received AAVrg-FLEX-dtA (Fig. 2D). Importantly, measurement of ACh levels revealed a significant reduction in hepatic ACh content in the experimental mice, whereas there was no difference in plasma ACh levels between the groups (Fig. 2E and F). These results support the interpretation that our experimental approach effectively ablates parasympathetic cholinergic neurons innervating the liver.

We then examined whether ChAT^{Cre} mice lacking parasympathetic cholinergic neurons innervating the liver responded differently to exposure to a high-fat diet (HFD) compared with the control group. We found a significant difference in body weight gain between the control and experimental groups during high-fat diet feeding for 10 weeks (Fig. 2G). The experimental mice gained significantly less than the controls during high-fat diet feeding. This reduction was closely associated with a significant reduction in fat mass in the experimental mice. In contrast, lean mass was similar in both the groups (Fig. 2H). When we compared adipose tissue mass collected from controls with that of adipose tissue from the

experimental group, we found a significant decrease in the mass of inguinal white adipose tissue (ingWAT) (Fig. 2I) and interscapular brown adipose tissue (iBAT) (Fig. S3A). Both the groups consumed the same amount of food during the light and dark phases (Fig. S4A). Given the absence of any difference in energy intake, the reduction in body weight may be attributed to an increase in energy expenditure. To measure the metabolic rate, we placed the animals in metabolic cages at 10 weeks of high-fat diet feeding. We observed that the experimental mice consumed more oxygen and produced more carbon dioxide in the dark phase than the controls (Fig. S4B and C). These results led to an increase in total energy expenditure in the experimental mice (Fig. S4D). The respiratory exchange ratio was similar between the groups (Fig. S4E). Interestingly, the experimental mice displayed an increase in locomotor activity during the dark period (Fig. S4F and G). Taken together, deleting liver-projecting cholinergic neurons appears to play a significant role in preventing diet-induced obesity through elevated energy expenditure.

Loss of parasympathetic cholinergic neurons innervating the liver improves insulin tolerance in male mice fed HFD

We assessed if deleting parasympathetic cholinergic neurons innervating the liver influences glucose homeostasis in mice fed HFD as the liver plays a major role in regulating systemic glucose homeostasis (*30*). The primary screening method for glucose intolerance and insulin sensitivity is the measurement of blood glucose and insulin levels. Basal (non-fasting) glucose levels were lower in $ChAT^{Cre}$ mice receiving AAVrg-FLEX-dtA injection than in the controls (Fig. S5A). The loss of DMV cholinergic neurons innervating the liver significantly reduced fasting glucose levels (Fig. S5B).

To examine if $ChAT^{Cre}$ mice without parasympathetic cholinergic neurons innervating the liver display a change in the ability to dispose of a glucose load, we performed intraperitoneal glucose tolerance tests (i.p.GTT) and found no significant difference in blood glucose levels in response to a bolus of glucose (i.p. 2 g/kg) between the groups (Fig. S5C and D). However, experimental mice exhibited increased insulin sensitivity (Fig. S5E). Blood glucose levels during the insulin tolerance tests (ITT) (i.p. 1 U/kg) were significantly lower in $ChAT^{Cre}$ mice injected with AAVrg-FLEX-dtA than in controls (Fig. S5E). In addition, improved insulin tolerance in the experimental group was associated with reduced plasma insulin levels relative to those in the controls (Fig. S5F). Therefore, the loss of DMV cholinergic input to the liver improved insulin sensitivity in $ChAT^{Cre}$ male mice fed HFD.

Parasympathetic cholinergic regulation of hepatic lipid metabolism

Insulin resistance is closely related to NAFLD in humans (*31, 32*). We investigated whether improved insulin resistance may be related to reduced hepatic steatosis in $ChAT^{Cre}$ mice without parasympathetic cholinergic neurons innervating the liver during high-fat feeding. To address this question, we first investigated if there are differences in the liver histology between the groups. Liver tissues were labeled with liver zonation markers such as the pericentral marker glutamine synthetase (GS)

and the periportal marker E-cadherin (E-cad) (*33*). The expression pattern of these zonation markers in the livers of the control group fed a standard chow diet demonstrated that GS- and E-cad-positive areas were clearly separated in the liver (Fig. S6A). Interestingly, high-fat feeding robustly reduced E-cad expression in periportal hepatocytes in the livers of control mice compared to control mice fed a standard chow diet (Fig. 3A), consistent with disrupted E-cad expression in chronic liver disease in mice (*34*). Surprisingly, deleting the parasympathetic cholinergic input to the liver in $ChAT^{Cre}$ mice fed HFD restored the expression of E-cad in periportal hepatocytes (Fig. 3B). In contrast, GS was similarly expressed in pericentral hepatocytes in both control and experimental mice fed HFD (Fig. 3A and B).

Hematoxylin and eosin (H & E) staining revealed a clear difference in the macroscopic appearance of the livers of $ChAT^{Cre}$ mice receiving AAVrg-FLEX-GFP and AAVrg-FLEX-dtA. Control mice exhibited an increased number of large and small lipid droplets and ballooned hepatocytes compared to experimental mice (Fig. 3C and D). Oil Red O staining further showed that $ChAT^{Cre}$ mice without DMV cholinergic neurons innervating the liver contained fewer lipid droplets in the liver than controls (Fig. 3E and F). Our results suggest that parasympathetic cholinergic input to the liver regulates hepatic steatosis during high-fat diet feeding.

As there was a lack of lipid droplets in the livers of the experimental mice, we measured the hepatic and plasma triglyceride (TG) levels. $ChAT^{Cre}$ mice without parasympathetic cholinergic neurons innervating the liver on high-fat feeding exhibited reduced TG levels in the liver compared to controls (Fig. 3G). This was associated with decreased plasma TG levels (Fig. 3G). Reverse transcription-quantitative polymerase chain reaction (RT-qPCR) analysis of liver tissues revealed a significant decrease in the expression of the lipogenic transcription factor sterol regulatory element-binding protein 1-c (*Srebp-1*) in the experimental mice relative to the controls. The experimental mice also exhibited downregulation of its target genes, including acetyl-coenzyme A carboxylase 1 (*Acaca*), fatty acid synthase (*Fasn*), stearoyl-CoA desaturase-1 (*Scd1*) (Fig. 3H). In addition, the $ChAT^{Cre}$ mice without parasympathetic cholinergic input to the liver had increased expression of peroxisome proliferator-activated receptor alpha (PPAR-α), the central transcriptional regulator of fatty acid oxidation relative the control group. As a result, there was increased carnitine palmitoyltransferase 1a (*Cpt1a*) and acyl-CoA dehydrogenase medium chain (*Acadm*) mRNA expression in the experimental mice relative to controls (Fig. 3H).

Hepatic vagal denervation leads to an increase in hepatic interleukin 6 (*Il6*) gene expression in mice, which subsequently modulates the expression of hepatic gluconeogenic enzymes (*35*). In our experiments, where selective deletion of liver-projecting cholinergic neurons was carried out, we observed a significant decrease in *Il6* gene expression (Fig. S7A). Importantly, there was no significant difference in gluconeogenic gene expression in the liver of the experimental and control

groups (Fig. S7A). In addition, we examined whether the loss of parasympathetic cholinergic innervation alters the sympathetic input to the liver. Immunostaining with an anti-tyrosine hydroxylase (Th) antibody revealed no detectable difference in the Th-positive nerve fibers (Fig. S8A and B). Moreover, hepatic norepinephrine levels were similar between the groups (Fig. S8C). Collectively, these results support the interpretation that parasympathetic cholinergic neurons innervating the liver play a critical role in hepatic lipid metabolism during high-fat diet feeding.

In contrast to male mice, C57BL/6 female mice were less likely to develop DIO and hyperglycemia than C57BL/6 male mice during high-fat feeding (*36-40*). In line with these prior findings, we found that control female mice did not develop DIO or hyperglycemia (Fig. S9A-F). Hepatic cholinergic loss of function had no effect on body weight or glucose homeostasis (Fig. S9A-F). In other words, the two groups did not display any notable differences in body weight, food intake, body composition, blood glucose levels, GTT, and ITT compared with the controls (Fig. S9A-F). In addition, high-fat feeding did not cause any changes in liver histology or fat accumulation in both control and experimental females (Fig. S9I-K). In fact, hepatic steatosis was also less common in C57BL/6 females than in males during high-fat feeding (*41-43*). Hence, we focused our further analyses on male mice.

ChAT^{Cre} mice without DMV cholinergic neurons innervating the liver exhibit beiging of ingWAT

WAT does not receive parasymapathetic cholinergic innervation in rodents (*44, 45*). Moreover, separate DMV cholinergic neuron subtypes appeared to have distinct targets even in the same organ such as the glandular stomach (*2*), suggesting that there are liver-specific DMV cholinergic neurons. These prior studies led us to hypothesize that parasympathetic cholinergic input to the liver may play a role in the crosstalk between the liver and WAT. In fact, short- and long-term increased lipolysis in WAT results in hepatic steatosis in fasted and insulin-resistant mice (*20, 46*). Interestingly, the fat mass in ChAT^{Cre} mice without DMV cholinergic neurons innervating the liver was lower than that in the controls (Fig. 2H). Hence, we examined whether there are metabolic alterations in WAT, particularly in ingWAT, which has a beiging capacity (*47*). We found that the size of the ingWAT in the experimental mice was smaller than that in the control mice (Fig. 4A). Histological analysis of ingWAT further revealed an increase in large-sized adipocytes in control mice compared to the experimental groups (Fig. 4B). In other words, there was a significant reduction in adipocyte area in ChAT^{Cre} mice without DMV cholinergic neurons innervating the liver (Fig. 4C and D), suggesting that a loss of DMV cholinergic input to the liver prevents ingWAT hypertrophy.

We asked if these unexpected results are associated with the beiging of ingWAT. RT-qPCR analysis revealed that deleting DMV cholinergic neurons innervating the liver significantly upregulated the expression of Peroxisome proliferator-activated receptor-gamma coactivator (PGC)-1alpha (PGC1α) in ingWAT, which is required for the expression of mitochondrial biogenesis and thermogenic

genes in brown fat cells (*48, 49*) (Fig. 4E). Likewise, the expression of PR (PRD1-BF1-RIZ1 homologous)-domain containing 16 (PRDM16), a transcription factor that plays a key role in browning and thermogenesis of subcutaneous WAT (*50*), was significantly increased in experimental mice relative to controls (Fig. 4E). The upregulation of these genes was associated with a robust increase in the mRNA expression of uncoupling protein 1 (*Ucp1*), iodothyronine deiodinase 2 (*dio2*), and cell death-inducing DFFA-like effector A (*Cidea*) (Fig. 4E). Western blotting and immunostaining further showed an increase in UCP1 protein levels in ingWAT of $ChAT^{Cre}$ mice receiving AAVrg-FLEX-dtA to the liver (Fig. 4F and G). In addition, daily measurement of ingWAT temperature revealed a significant elevation in the ingWAT temperature of the experimental mice in the dark phase (Fig. 4H). These data support that a loss of parasympathetic cholinergic neurons innervating the liver induces beiging of ingWAT with an increase in thermogenesis.

WAT lipolysis in obesity contributes to fatty acid and glycerol overloads in the liver (*51*). This lipid influx can cause hepatic TG synthesis, which results in NAFLD (*52*). We examined if ablation of the DMV cholinergic input to the liver reduced HSL-mediated lipolysis in ingWAT. Western blot analysis of ingWAT showed a reduction in phospho-HSL levels in the experimental mice (Fig. 4I). Additionally, we found lower levels of plasma glycerol in experimental mice than in control mice (Fig. 4J). Collectively, the loss of hepatic cholinergic innervation upregulated the expression of thermogenic genes while reducing lipolysis in ingWAT.

Increased bile acid synthesis and secretion in $ChAT^{Cre}$ mice lacking DMV cholinergic neurons innervating the liver induces ingWAT beiging via TGR5.

What causes the beiging of the ingWAT in mice without DMV cholinergic neurons innervating the liver? It has been shown that bile acid and its cognate receptor TGR5 are involved in WAT browning (*22, 53*). We thus investigated whether the loss of function of liver-innervating cholinergic neurons changes the expression of genes related to bile acid synthesis, such as *Cyp7a1* and *Cyp7b1* (Fig. 5 A). We found that hepatic cholinergic loss of function upregulated expression of the *Cyp7b1* gene involved in an alternative bile acid synthesis pathway (*54*) (Fig. 5A). Furthermore, our spatial transcriptomic analysis of the liver revealed that $ChAT^{Cre}$ mice without DMV cholinergic neurons innervating the liver displayed a trend toward an increase in *Cyp7b1* gene expression in all three zones (Fig. 5B), whereas *Cyp7a1* expression was not altered, as observed in qPCR experiments (Fig. 5A and 5B). Elevated *Cpy7b1* expression led to a substantial increase in fasting serum bile acid levels in $ChAT^{Cre}$ mice that received AAVrg-FLEX-dtA. (Fig. 5C). We performed a further analysis of the fasting serum bile acid profiles in control and experimental mice and observed a significant increase in primary bile acids such as cholate and chenodeoxycholate resulting from the loss of hepatic cholinergic input (Fig. 5D).

We then investigated whether there are any alterations in the expression of its cognate receptor TGR5 in ingWAT of the experimental mice. We observed elevated levels of TGR5 gene and protein expression in the ingWAT of experimental mice compared to that in the control group. (Fig. 6A), suggesting that the elevated levels of serum bile acids and increased expression of *Tgr5* in the ingWAT would lead to ingWAT beiging in experimental mice. To investigate this possibility, we knocked down *Tgr5* exclusively in ingWAT by administering *Tgr5* siRNA or control siRNA into the ingWAT of $ChAT^{Cre}$ mice without liver-innervating cholinergic neurons (Fig. 6B). Ten weeks post viral infection, we collected and performed RT-qPCR and Western blot analyses and found that the *Tgr5* gene and protein levels in ingWAT were significantly reduced following *Tgr5* siRNA injection (Fig. 6C), indicating that our approach effectively knocked down *Tgr5* expression. Under these experimental conditions, we observed that *Tgr5* knockdown in ingWAT resulted in complete reversal of the effect of the loss of hepatic cholinergic function on body weight gain during high-fat diet feeding. In other words, we observed a significant increase in body weight and total fat mass in mice receiving AAVrg-FLEX-dtA to the liver and Tgr5 siRNA to ingWAT, compared to mice receiving AAVrg-FLEX-dtA to the liver alone (Figure 6D and E). These mice displayed a significant increase in liver, inguinal, interscapular, gonadal, and perigonadal adipose tissue masses (Fig. 6F). Histological analysis of ingWAT further revealed that there was an increase in the number of large-sized adipocytes and crown-like structures in experimental mice that received *Tgr5* siRNA (Fig. 6J). This was associated with a significant increase in the adipocyte area (Fig. 6H and I). Therefore, TGR5 in ingWAT seems to exert a considerable impact on whole-body energy metabolism during high-fat diet feeding.

We then examined if *Tgr5* knockdown alters HSL-mediated lipolysis in ingWAT. Western blot analysis of the ingWAT revealed an increase in phospho-HSL levels (Fig 7A), which resulted in elevated levels of plasma glycerol (Fig. 7B). Given the established correlation between elevated plasma glycerol levels and lipid accumulation in the liver, we investigated if *Tgr5* knockdown causes hepatic steatosis. We observed the presence of large lipid droplets and ballooned hepatocytes in liver sections of mice administered *Tgr5* siRNA (Figure 7C). Oil Red O staining further confirmed the accumulation of lipids in the livers of mice receiving *Tgr5* siRNA in the ingWAT (Figure 7D). In addition, knockdown of the *Tgr5* gene in ingWAT of $ChAT^{Cre}$ mice without DMV cholinergic neurons to the liver caused a significant rise in hepatic TG content, which is indicative of enhanced lipid accumulation in the liver. (Fig. 7E). Taken together, our results support the interpretation that crosstalk between the liver and ingWAT through elevated bile acid signaling plays a crucial role in maintaining the lipid metabolism balance in both the liver and ingWAT (Fig. 7F).

Discussion

The present study provides neuroanatomical and physiological evidence for the existence of the cholinergic system in the mouse liver. Our findings demonstrated that DMV cholinergic neurons sent direct axonal projections to the hepatocytes and cholangiocytes. Numerous vAChT- and ChAT-positive nerve terminals were also distributed throughout the liver parenchyma and hepatocytes also expressed muscarinic ACh receptors. 3D imaging analysis of the cleared liver tissue further revealed the presence of cholinergic nerve terminals around the portal vein and throughout the liver parenchyma. The loss of hepatic cholinergic function resulted in a significant decrease in body weight compared to the control group that was associated with an elevated energy expenditure. Additionally, fat mass in $ChAT^{Cre}$ mice administered AAVrg-FLEX-dtA was significantly lower than that in control mice. $ChAT^{Cre}$ mice, which lack DMV cholinergic input to the liver, exhibited an improvement in insulin sensitivity. Furthermore, the absence of cholinergic input to the liver prevented the development of hepatic steatosis during high-fat diet feeding, which was closely linked to the browning of ingWAT. $ChAT^{Cre}$ mice without cholinergic input to the liver displayed elevated bile acid synthesis, primarily through the CYP7B1-mediated alternative pathway, leading to elevated serum bile acid levels. Importantly, the experimental mice exhibited elevated *Tgr5* gene expression in ingWAT, which was found to be critical in mediating the beneficial effects of the loss of hepatic cholinergic function. Specifically, knockdown of the *Tgr5* gene in ingWAT completely abolished these beneficial effects and led to the reappearance of hepatic steatosis in the experimental groups. These findings suggest that TGR5 is a crucial mediator of the metabolic benefits conferred by loss of hepatic cholinergic function. Taken together, our results suggest that parasympathetic cholinergic input to the liver plays an essential role in bile acid synthesis and secretion. This interorgan crosstalk via bile acids is critical for the development of systemic insulin resistance and hepatic steatosis.

Accumulated studies have shown that parasympathetic innervation to the liver controls hepatic glucose output, lipid metabolism, and bile formation (*6, 7, 9, 19, 55*). However, the paucity of detailed neuroanatomical information on parasympathetic innervation to the liver raised doubts about its role in controlling hepatic metabolism (*14, 15*). In addition, although hepatic branch vagotomy altered multiple physiological processes, including glucose homeostasis (*6, 55*), hepatic lipid metabolism (*7, 19*), and hepatic inflammatory response (*9*), studies with hepatic branch vagotomy do not provide conclusive support for the parasympathetic cholinergic contribution to liver function. In fact, the hepatic branches of the vagus nerve also includes vagal sensory nerves that send interoceptive information from the liver to the brain. Nevertheless, several research groups have also clearly described the presence of DMV cholinergic neurons innervating the liver using virus-mediated tracing methods (*11-13*). Importantly, our findings, which were obtained using anterograde tracing techniques in combination with 2D immunostaining and 3D imaging of cleared liver tissue, provide robust evidence for the existence of

direct synaptic connections between DMV cholinergic neurons and hepatocytes. It is evident that hepatocytes received nerve terminals that were positive for both vAChT and ChAT. Selective elimination of DMV cholinergic neurons that innervate the liver resulted in a significant decrease in the number of vAChT-positive nerve terminals and hepatic ACh levels. The discrepancy between recent 3D imaging studies (*14, 15*) and ours may be partly due to differences in the morphology of postganglionic and preganglionic neurons. Specifically, while both sympathetic postganglionic and sensory neurons (particularly c-fibers) possess unmyelinated nerve fibers, the nerve fibers of the parasympathetic cholinergic preganglionic neurons are myelinated (*56, 57*). The myelin sheath may impede the staining of cholinergic nerve fibers in the liver parenchyma. In fact, we detected cholinergic nerve terminals, but not nerve fibers, whereas TH-positive nerve fibers were clearly visible in the liver parenchyma. In addition to our prior functional analysis (*12*), our current neuroanatomical results strongly support the fact that the liver is an important downstream target of the parasympathetic cholinergic efferent neurons.

As expected, $ChAT^{Cre}$ male mice fed a high-fat diet exhibited hepatic steatosis (*58*). Elevated blood glucose levels and hepatic insulin resistance drove hepatic *de novo* lipogenesis in humans (*31, 32*). $ChAT^{Cre}$ mice fed HFD displayed elevated basal and fasting glucose levels and higher basal insulin levels compared to the experimental groups. These hyperglycemic and hyperinsulinemic conditions during high-fat feeding clearly led to hepatic steatosis in control mice. Notably, the complete deletion of the parasympathetic cholinergic input to the liver resulted in the reversal of the detrimental effects of high-fat feeding on insulin sensitivity and hepatic fat accumulation. These beneficial effects were partly attributed to reduced hepatic *de novo* lipogenesis and enhanced fatty acid oxidation in the livers of $ChAT^{Cre}$ mice, which lack the DMV cholinergic innervation. In other words, a loss of DMV cholinergic innervation to the liver resulted in decreased expression of genes associated with lipogenesis while increasing the expression of genes involved in fatty acid oxidation, leading to lower levels of triglycerides. Our current findings support a substantial role of parasympathetic cholinergic innervation to the liver in the control of hepatic lipid metabolism under obesogenic conditions.

Simple hepatic steatosis resulted from an imbalance between the delivery and production of fat in the liver and its subsequent secretion and metabolism (*59*). Excessive dietary fat led to increased plasma concentrations of TGs and free fatty acids (FFAs), resulting in increased uptake into hepatocytes (*60*). In our preparations, both groups consumed the same amount of food, suggesting that there might be no significant difference in the total fat intake per day. Additional sources of fatty acids include lipolysis of TGs stored in adipocytes, which is primarily regulated by insulin (*61*). Insulin-induced suppression of lipolysis in adipocytes is the major mechanism by which insulin regulates systemic lipid metabolism. The net effect of insulin on adipocytes is that it normally takes up more FFAs from lipoproteins and exports fewer FFAs (*60*). In contrast, insulin resistance depressed both of these functions (*60*). $ChAT^{Cre}$ mice,

which lack DMV cholinergic neurons innervating the liver, displayed enhanced insulin sensitivity compared with the control group. This metabolic profile, including decreased adiposity, lower levels of plasma glycerol, and reduced fat mass, may contribute to the improved insulin sensitivity observed in experimental mice. In particular, improved insulin resistance in adipocytes would significantly limit the flow of FFAs and glycerol to the liver, thus preventing the development of hepatic steatosis in $ChAT^{Cre}$ mice without cholinergic innervation to the liver during high-fat feeding.

We should also emphasize that the loss of hepatic cholinergic innervation induced beiging of ingWAT. This browning process promotes glucose uptake and contributes significantly to systemic glucose disposal, which can ultimately lead to improved insulin sensitivity (*51*). Signaling molecules secreted by hepatocytes, such as bile acids, can cause WAT browning via TGR5 (*22, 53, 62*). Daily administration of the TGR5 agonist for 1 week significantly reduced subcutaneous WAT (scWAT) mass and induced the expression of scWAT browning marker genes such as *Ucp1* and *Cidea* (*22*). Similarly, $ChAT^{Cre}$ mice lacking liver-projecting cholinergic neurons displayed a significant reduction in WAT mass and adipocyte size. Furthermore, these mice showed an increase in thermogenic gene and protein expression in ingWAT, leading to elevated nocturnal ingWAT temperature. Importantly, the loss of hepatic cholinergic innervation upregulated *Cyp7b1*, which is involved in the control of cholesterol metabolism and bile acid production in the liver (*54*), and elevated fasting serum bile acid levels. Our findings revealed that both hepatocytes and bile ducts, which are responsible for controlling bile flow and formation, received cholinergic innervation. Furthermore, it has been demonstrated that the muscarinic ACh receptors expressed on cholangiocytes play a role in regulating bile flow (*24*). Interestingly, there are molecularly distinct subtypes of DMV cholinergic neurons with different targets within the glandular stomach (*2*). It is plausible that distinct subsets of DMV cholinergic neurons innervate hepatocytes and cholangiocytes and that these two distinct populations of neurons regulate bile acid synthesis and secretion. Moreover, our findings suggest that the loss of parasympathetic innervation did not have any impact on sympathetic input to the liver. Hence, prior studies and our findings strongly support the fact that the parasympathetic cholinergic system in the liver may play an important role in crosstalk between the liver and other internal organs.

Communication between ingWAT and other organs, including the liver and muscle, is critical for systemic metabolism (*61*). In the current study, we found that crosstalk between the liver and ingWAT via bile acids significantly contributed to the progression of hepatic steatosis. In fact, silencing *Tgr5* in the ingWAT completely reversed the beneficial effects of the loss of hepatic cholinergic innervation. For instance, *Tgr5* knockdown resulted in enlarged adipocytes, leading to hypertrophy. Surprisingly, knockdown of *Tgr5* restricted to ingWAT induced lipid accumulation in the livers of $ChAT^{Cre}$ mice without cholinergic innervation to the liver. In other words, the loss of hepatic cholinergic innervation

failed to prevent the onset of hepatic steatosis following silencing of *Tgr5* in ingWAT, suggesting an important contribution of ingWAT to the development of hepatic steatosis. In fact, knockdown of *Tgr5* in ingWAT elevated plasma glycerol levels, indicating a role of TGR5 in regulating lipolysis in ingWAT. While our study provides evidence for crosstalk between the liver and ingWAT via TGR5, it is possible that TGR expressed in central neurons may also play a role in the observed effects. It has been well described that activation of hypothalamic TGR5 suppressed food intake and prevented diet-induced obesity (*63, 64*).

In summary, our results strongly support the existence of parasympathetic cholinergic input to the liver. Parasympathetic cholinergic input to the liver plays an essential role in bile acid synthesis and secretion. Bile acid-mediated crosstalk between the liver and WAT is critical in the development of systemic insulin resistance and eventually, hepatic steatosis in obese conditions. Targeting parasympathetic cholinergic input to the liver could be an alternative treatment for systemic insulin resistance and its related hepatic steatosis in obesity.

Materials and Methods

Ethics statement

All mouse care and experimental procedures were approved by the Institutional Animal Care Research Advisory Committee of the Albert Einstein College of Medicine and performed in accordance with the guidelines described in the NIH Guide for the Care and Use of Laboratory Animals. Viral injections were performed under isoflurane anesthesia.

Animals

Eight-nine-week-old ChAT^{Cre} mice were purchased from Jackson Laboratory (JAX stock # 006410) (*65*). We backcrossed them to C57BL/6J mice for several generations, and the mutant mice were bred together to make this line homozygous. Mice were housed in cages under conditions of controlled temperature (22 °C) with a 12:12 h light-dark cycle and fed a high-fat diet (HFD; Research Diets, D12492; 20% calories by carbohydrate, 20% by protein, and 60% by fat) for 10-12 weeks, with water provided *ad libitum*. Mice were euthanized with an overdose of isoflurane at the end of the experiment.

Western Blotting

Proteins were isolated from the liver using CelLytic™ MT (Sigma, C3228) in the presence of a protease inhibitor/phosphatase inhibitor cocktail (Thermo Fisher Scientific, 78443). Proteins from the ingWAT were extracted using a protein extraction kit for adipocyte tissue (Invent, AT-022).

Protein concentrations were determined using the BCA Protein Assay Kit (Thermo Fisher Scientific, 23225). Proteins (30-50 ug) were prepared by adding laemmli sample buffer (Bio-Rad, 1610747) and heated at 95^{0}C for 5min. The samples were then separated using 10% SDS-PAGE and transferred to a polyvinylidene fluoride (PVDF) membrane. The PVDF membrane was incubated with 5% w/v non-fat dry milk or 5% BSA for 1 h at room temperature and immunoblotted with anti-HSL (phospho-serine 660) (1:1000, Cell Signaling Technology, 45804S), anti-HSL (1:1000, Cell Signaling Technology, 4107), rabbit anti-UCP1(1:1000, Abcam, ab234430), rabbit anti-CHRM1 (1:200, Alomone Labs, AMR-001), rabbit anti-CHRM2 (Alomone Labs, AMR-002), rabbit anti-CHRM3 (Alomone labs, AMR-006), rabbit anti-CHRM4 (Alomone labs, AMR-004), rabbit anti-CHRM5 (Alomone Labs, AMR-005), and rabbit anti-β-actin (Cell Signaling, 4970S) antibodies. The specificity of anti-CHRM1-5 antibodies was tested by preincubation with the blocking peptide (CHRM1 with BLP-MR001, CHRM2 with BLP-MR002, CHRM3 with BLP-MR006, CHRM4 with BLP-MR004, and CHRM5 with BLP-MR005). Following incubation with primary antibodies, the membrane was washed three times in TBS-T and then incubated with an anti-rabbit IgG, HRP-linked antibody (1:10,000, Cell Signaling Technology, 7074) for 2 h at room temperature. ECL reagents were applied to the membrane and protein bands were detected using an Odyssey Fc imaging system (Li-COR).

Immunostaining to examine the hepatic cholinergic system

To examine DMV cholinergic neurons innervating the liver, $ChAT^{Cre}$ mice received an AAV.Php.eB-flex-tdTomato (titer; $1.9x10^{13}$ pfu/ml, Addgene 28306-PHP.eB) injection into the liver. We also injected AAV-phSyn1(s)-FLEX-tdTomato-T2A-SypGFP-WPRE (Addgene 51509-AAV1) into the DMV (500 nl of 4 x 10^{12} pfu/ml per site; coordinate; AP: -7.5 mm, ML: +/-1 mm, DV: -3.5 mm) to label cholinergic nerve terminals in the liver. Mice were killed 5 and 10 weeks post-viral inoculation.

Mice were anesthetized with isoflurane (3%) and transcardially perfused with pre-perfusion solution (9 g NaCl, 5 g sodium nitrate, 10,000 U heparin in 1L distilled water) followed by 4% paraformaldehyde solution. Liver sections were stained with a rabbit anti-GFP antibody (Rockland, 600-401-215, 1:500) to visualize cholinergic nerve terminals. Brainstem sections were labeled with rabbit anti-RFP (Rockland, 600-401-379, 1:500) and goat anti-ChAT antibodies (Millipore, AB144P, 1:200). The expression of muscarinic ACh receptors CHRM2 and 4 was examined using rabbit anti-CHRM2 (Alomone, AMR-002, 1:200) and rabbit anti-CHRM4 (Alomone, AMR-004, 1:200) antibodies. Cholinergic nerve terminals were stained with goat anti-vAChT (Millipore, ABN100) and goat anti-ChAT (Millipore, AB144P) antibodies. The tissue samples were incubated with AlexaFluor 568 donkey anti-goat IgG (Invitrogen, A11057, 1:200), AlexaFluor 568 donkey anti-rabbit IgG (Invitrogen, A11011, 1:200), and AlexaFluor 488 donkey anti-rabbit IgG (Invitrogen, A21206, 1:200). The tissues were washed, dried, and mounted with VECTASHIELD medium containing DAPI. Images were acquired using a Leica SP8 confocal microscope.

Clear, unobstructed brain imaging cocktails and computational analysis (CUBIC) tissue clearing of the brainstem and liver tissues

The CUBIC method (*66*) was used to clear liver and brainstem tissues. Mice were perfused with 4% (w/v) paraformaldehyde (PFA) in PBS. Liver and brain tissues were collected and post-fixed in 4% PFA at 4C° for 24 h. Tissue samples were sectioned using a vibratome at a thickness of 300 mm. The sections were immersed in CUBIC reagent 1(25wt% Urea, 25wt% Quadrol, 15wt% Triton X-100) with gentle shaking at 37C° for 3 days. After decolorization (transparent tissues), the sections were washed with PBS three times at RT for 2 h and then incubated in a blocking solution composed of 1% donkey serum, 0.5% BSA, 0.3% Triton X-100, and 0.05% sodium azide for 3 h at RT with rotation. The tissue samples were incubated with goat anti-ChAT (Millipore, AB144P, 1:200), rabbit anti-RFP (Rockland, 200-301-379 1:200), and rabbit anti-GFP (Rockland, 600-401-215, 1:200) antibodies for 5 days at RT with mild shaking, and washed three times with PBS (each for at least 2 h). Following wash-out, the tissue samples were incubated with AlexaFluor 568 donkey anti-goat IgG (1:200, Invitrogen, A11057), AlexaFluor 568 donkey anti-rabbit IgG (1:200, Invitrogen, A11011), and AlexaFluor 488 donkey anti-rabbit IgG (1:200, Invitrogen, A21206) for 3 days at room temperature. Tissues were washed and

immersed in CUBIC-reagent 2 (50wt% Sucrose, 25wt% Urea, 10wt% Triethanolamine, and 0.1%(v/v) Triton X-100) for 1 d and mounted with a mixture of mineral oil and silicone oil. Z-stack images were taken with a Leica SP8 confocal microscope, and 3D construction was performed with the AIVIA community (version 12.1).

Viral injection to delete DMV cholinergic neurons innervating the liver

pAAV-mCherry-FLEX-dtA (Addgene, 58536) was subcloned and packaged in an AAV serotype retrograde (Applied Biological Materials, Inc.). A total volume of 10 -20 ul of AAVrg-mCherry-FLEX-dtA (titer, >1 × 10^{12} pfu/ml) was injected into the livers of the $ChAT^{Cre}$ mice. AAVrg-FLEX-GFP viruses (titer, >1x10^{13} pfu/ml) were used as the controls.

To quantify cell death over time, the mice were killed 10-12 weeks after viral inoculation. Mice were anesthetized with isoflurane (3%) and transcardially perfused with PBS and heparin, followed by 10% neutral buffered formalin solution (Sigma, HT501128). Brainstem and liver tissues were embedded in paraffin to create paraffin blocks. Paraffin blocks were cut into 10 um sections for the brainstem and 5 µm sections for liver tissues at our histology and comparative pathology core facility.

Coronal sections of the brainstem from approximately −7.2 to −7.6 mm posterior to bregma were stained with an anti-ChAT antibody (Millipore, AB144P). Cell counting of DMV cholinergic neurons was performed using the ImageJ software (version FIJI). The adipocyte cell area was measured using the Adiposoft plugin (version 1.16) in the Image J software.

Measurement of body weight, body composition, and blood glucose

Body weight was measured weekly at 9 am. Body composition for fat mass and fat-free mass was assessed by ECHO MRI at our animal physiology core. Blood samples were collected from the mouse tail, and a small drop of blood was placed on the test strip of a glucose meter. Non-fasting basal glucose levels were measured at 9:00 am. Fasted blood glucose levels were measured after overnight fasting at 10 weeks post-viral injection.

Assessment of energy expenditure and locomotor activity

To examine if the loss of function of hepatic cholinergic input regulates energy expenditure and locomotor activity, we performed indirect calorimetry on mice fed HFD for 10 weeks. Mice were individually housed in the calorimeter cages and acclimated to the respiratory chambers for at least 2 days prior to gas exchange measurements. Indirect calorimetry was performed for 3 days at the end of 10 weeks using an open-circuit calorimetry system. O_2 consumption and CO_2 production were measured for each mouse at 10-min intervals over a 24-h period. The respiratory exchange ratio was calculated as the ratio of CO_2 production over O_2 consumption. Since there was no difference in food intake, VO_2 was

normalized for body lean mass. Locomotor activity in X-Y and Z planes was measured by infrared beam breaks in the calorimetry cages.

Assessment of glucose tolerance and insulin tolerance

For GTT, the experimental and control mice were fasted for 15 h (6:00 pm–9:00 am) at 10 weeks post-viral inoculation. Sterile glucose solution was intraperitoneally administered at a concentration of 2 g/kg (glucose/body weight) at time 0. Blood glucose levels were measured at 15, 30, 60, 90, and 120 min after glucose injection. Blood glucose levels versus time after glucose injection were plotted, and the area under the curve was calculated and compared between the experimental and control groups.

For ITT, the mice were fasted for 4 h (9:00 am to 1:00 pm). Blood glucose levels were measured at 0, 15, 30, 60, 90, and 120 min following i.p. injection of insulin (1 U/kg). We immediately injected glucose (2 g/kg) if the mice appeared ill owing to insulin-induced hypoglycemia.

RT-qPCR analysis

Liver tissues were collected from the experimental and control groups 10-12 weeks post viral inoculation. Liver tissues were homogenized in Trizol reagent (ThermoFisher Scientific, 15596-018), and total RNAs were isolated according to the manufacturer's instructions. First-strand cDNAs were synthesized using the SuperScript III First-Strand synthesis kit (ThermoFisher Scientific, 18080-051). qPCR was performed in sealed 96-well plates with SYBR Green I master Mix (Applied Biosystems, A25742) using the Quant Studio 3 system (Applied Biosystems). qPCR reactions were prepared in a final volume of 20 ul containing 2 ul cDNAs, and 10 ul of SYBR Green master mix in the presence of primers at 0.5 uM. Glyceraldehyde 3-phosphate dehydrogenase *(Gapdh)* for liver and 18S ribosomal RNA (*18s rRNA*) for white adipocyte tissue were used as an internal control for quantification of each sample. Amplification was performed under the following conditions: denaturation at 95°C for 30 seconds, followed by 40 cycles of denaturation at 95°C for 30 seconds, and annealing/extension at 60°C for 1 minute.

We examined the following genes; *Srebp1c* (NM_001358315.1), *Chrebp* (NM_021455.5), *Acly* (NM_134037.3), *Acaca* (NM_133360.3), *Fasn* (NM_007988.3), *Scd1* (NM_009127.4), *Ppara* (NM_011144.6), *Prdm16* (NM_027504), *Cpt1a* (NM_013495.2), *Cpt2* (NM_009949.2), *Acadm* (NM_007382.5), *Acadl* (NM_007381.4), *G6pase* (NM_008061.4), *Pck1* (NM_011044.3), *Slc2a2* (NM_031197.2), *Pgc1a* (NM_008904.3), *Ucp1* (NM_009463.3), *Dio2* (NM_010050.4), *Cidea* (NM_007702.2), *Gpbar1* (NM_174985.1), *Cyp7a1* (NM_007824), *Cyp7b1* (NM_007825) (Table S1). All the primer sequences will be validated with "Primer BLAST" primer design program to ensure specificity for the target gene. Melt curves and gel electrophoresis were analyzed to confirm the specificity of the PCR products. Relative gene expression was determined using a comparative method ($2^{-\Delta\Delta CT}$).

Spatial Transcriptomics

Livers were snap-frozen in liquid nitrogen and thawed briefly on ice, followed by embedding in a cryomold (Sakura, 4565) filled with Neg-50 (Epredia, 6502). The cryomold was then frozen by placing into a container with pre-chilled 2-methylbutane on dry-ice. The samples were cryosectioned (Cryostar NX70 Cryostat, -18C for blade, -18 ºC for specimen head, set at 10mm thickness) and placed on a pre-chilled Visium Spatial Gene Expression Slide (10x Genomics, PN-2000233). The tissue sections were processed following 10x Genomics protocols (PN-1000187, PN-1000215). The adaptors and sequencing primers were obtained from Illumina. The libraries were sequenced by Novogene using the NovaSeq 6000 (PE150) instrument targeting 80,000 reads per spot. Fastq files were aligned against mouse mm10 reference and histology images were processed with Spaceranger (2.0.0). Pericentral, mid-zone and periportal clusters were identified based on Graph-Based clusters and known zonation markers (*Cyp2e1*, *Glul*, *Gulo* for pericentral, *Cyp2f2*, *Hsd17b13*, *Sds* for periportal). Violin plots were generated using Loupe Browser (6.4.1).

Measurement of hepatic and plasma TG and ACh levels

Liver samples were harvested from mice with or without liver-innervating cholinergic neurons. Tissue samples were weighed and homogenized in 1 mL of diluted NP-40 solution to solubilize triglycerides. The samples were centrifuged at 16,000 × g to remove insoluble material. The TG levels were measured using a TG assay kit (Cayman Chemical, 10010303).

For the acetylcholine assay, liver tissues were homogenized in PBS. The homogenates were then centrifuged at 5,000 g for 5 min. The supernatants were collected, and ACh levels were determined using an acetylcholine ELISA kit (Novus, NBP2-66389).

Measurement of plasma insulin levels and fasting serum bile acid levels

Blood samples from the experimental and control groups were collected from the retroorbital plexus using heparinized capillary tubes. Whole blood was centrifuged at 12,000 × g for 10 min, and plasma was separated and stored at -20°C until use. Plasma insulin concentrations were determined using two-site sandwich ELISA kits (Mercodia, cat# 10-1247-0). To analyze fasting total bile acid levels in the serum, fasting blood samples were collected without anticoagulant and determined using mouse total bile acid (Crystal Biochem, Cat#80471). Bile acid profiling was performed at our metabolomic core facility.

Statistics

All statistical results are presented as the mean ± SEM. Statistical analyses were performed using GraphPad Prism, version 10.0. Two-tailed *t*-tests were used to determine the p-values for each pairwise comparison. The Mann-Whitney U test was performed to evaluate the differences in bile acid composition between the groups. Time-course comparisons between groups were analyzed using a two-

way repeated-measures analysis of variance (RM ANOVA) with Sidak's correction for multiple comparisons. Data were considered significantly different when the probability value was less than 0.05.

Reference cited:

1. E. Trefts, M. Gannon, D. H. Wasserman, The liver. *Curr Biol* **27**, R1147-R1151 (2017).
2. J. Tao *et al.*, Highly selective brain-to-gut communication via genetically defined vagus neurons. *Neuron*, (2021).
3. A. K. Fontaine *et al.*, Optogenetic stimulation of cholinergic fibers for the modulation of insulin and glycemia. *Sci Rep* **11**, 3670 (2021).
4. A. Standish, L. W. Enquist, J. A. Escardo, J. S. Schwaber, Central neuronal circuit innervating the rat heart defined by transneuronal transport of pseudorabies virus. *The Journal of neuroscience : the official journal of the Society for Neuroscience* **15**, 1998-2012 (1995).
5. R. C. Rogers, G. E. Hermann, Central connections of the hepatic branch of the vagus nerve: a horseradish peroxidase histochemical study. *J Auton Nerv Syst* **7**, 165-174 (1983).
6. A. Pocai, S. Obici, G. J. Schwartz, L. Rossetti, A brain-liver circuit regulates glucose homeostasis. *Cell metabolism* **1**, 53-61 (2005).
7. M. T. Hackl *et al.*, Brain leptin reduces liver lipids by increasing hepatic triglyceride secretion and lowering lipogenesis. *Nat Commun* **10**, 2717 (2019).
8. A. Niijima, Blood glucose levels modulate efferent activity in the vagal supply to the rat liver. *The Journal of physiology* **364**, 105-112 (1985).
9. T. Nishio *et al.*, Hepatic vagus nerve regulates Kupffer cell activation via alpha7 nicotinic acetylcholine receptor in nonalcoholic steatohepatitis. *J Gastroenterol* **52**, 965-976 (2017).
10. P. H. Bisschop, E. Fliers, A. Kalsbeek, Autonomic regulation of hepatic glucose production. *Compr Physiol* **5**, 147-165 (2015).
11. S. Stanley *et al.*, Identification of neuronal subpopulations that project from hypothalamus to both liver and adipose tissue polysynaptically. *Proceedings of the National Academy of Sciences of the United States of America* **107**, 7024-7029 (2010).
12. E. Kwon *et al.*, Optogenetic stimulation of the liver-projecting melanocortinergic pathway promotes hepatic glucose production. *Nat Commun* **11**, 6295 (2020).
13. F. Kreier *et al.*, Tracing from fat tissue, liver, and pancreas: a neuroanatomical framework for the role of the brain in type 2 diabetes. *Endocrinology* **147**, 1140-1147 (2006).
14. K. Liu *et al.*, Metabolic stress drives sympathetic neuropathy within the liver. *Cell metabolism* **33**, 666-675 e664 (2021).
15. C. Adori *et al.*, Disorganization and degeneration of liver sympathetic innervations in nonalcoholic fatty liver disease revealed by 3D imaging. *Sci Adv* **7**, (2021).
16. E. M. Brunt *et al.*, Nonalcoholic fatty liver disease. *Nat Rev Dis Primers* **1**, 15080 (2015).
17. R. Loomba, S. L. Friedman, G. I. Shulman, Mechanisms and disease consequences of nonalcoholic fatty liver disease. *Cell* **184**, 2537-2564 (2021).
18. M. Metz *et al.*, Leptin increases hepatic triglyceride export via a vagal mechanism in humans. *Cell metabolism* **34**, 1719-1731 e1715 (2022).
19. J. T. Yue *et al.*, A fatty acid-dependent hypothalamic-DVC neurocircuitry that regulates hepatic secretion of triglyceride-rich lipoproteins. *Nat Commun* **6**, 5970 (2015).
20. V. Azzu, M. Vacca, S. Virtue, M. Allison, A. Vidal-Puig, Adipose Tissue-Liver Cross Talk in the Control of Whole-Body Metabolism: Implications in Nonalcoholic Fatty Liver Disease. *Gastroenterology* **158**, 1899-1912 (2020).
21. B. R. Barrows, E. J. Parks, Contributions of different fatty acid sources to very low-density lipoprotein-triacylglycerol in the fasted and fed states. *J Clin Endocrinol Metab* **91**, 1446-1452 (2006).
22. L. A. Velazquez-Villegas *et al.*, TGR5 signalling promotes mitochondrial fission and beige remodelling of white adipose tissue. *Nat Commun* **9**, 245 (2018).
23. F. Wang, Z. Lu, X. Wang, Y. Zhang, Impaired vagus function in rats suppresses bile acid synthesis in the liver by disrupting tight junctions and activating Fxr-Fgf15 signaling in the intestine. *Biochem Biophys Res Commun* **495**, 1490-1496 (2018).

24. C. Elsing, C. Hubner, B. A. Fitscher, A. Kassner, W. Stremmel, Muscarinic acetylcholine receptor stimulation of biliary epithelial cells and its effect on bile secretion in the isolated perfused liver [corrected]. *Hepatology* **25**, 804-813 (1997).
25. K. Y. Chan *et al.*, Engineered AAVs for efficient noninvasive gene delivery to the central and peripheral nervous systems. *Nature neuroscience* **20**, 1172-1179 (2017).
26. J. Rossi *et al.*, Melanocortin-4 receptors expressed by cholinergic neurons regulate energy balance and glucose homeostasis. *Cell metabolism* **13**, 195-204 (2011).
27. R. B. Chang, D. E. Strochlic, E. K. Williams, B. D. Umans, S. D. Liberles, Vagal Sensory Neuron Subtypes that Differentially Control Breathing. *Cell* **161**, 622-633 (2015).
28. S. W. Oh *et al.*, A mesoscale connectome of the mouse brain. *Nature* **508**, 207-214 (2014).
29. Z. Wu, A. E. Autry, J. F. Bergan, M. Watabe-Uchida, C. G. Dulac, Galanin neurons in the medial preoptic area govern parental behaviour. *Nature* **509**, 325-330 (2014).
30. H. S. Han, G. Kang, J. S. Kim, B. H. Choi, S. H. Koo, Regulation of glucose metabolism from a liver-centric perspective. *Exp Mol Med* **48**, e218 (2016).
31. G. I. Smith *et al.*, Insulin resistance drives hepatic de novo lipogenesis in nonalcoholic fatty liver disease. *The Journal of clinical investigation* **130**, 1453-1460 (2020).
32. N. Kumashiro *et al.*, Cellular mechanism of insulin resistance in nonalcoholic fatty liver disease. *Proceedings of the National Academy of Sciences of the United States of America* **108**, 16381-16385 (2011).
33. R. P. Cunningham, N. Porat-Shliom, Liver Zonation - Revisiting Old Questions With New Technologies. *Front Physiol* **12**, 732929 (2021).
34. M. Hempel *et al.*, Pathological implications of cadherin zonation in mouse liver. *Cell Mol Life Sci* **72**, 2599-2612 (2015).
35. K. Kimura *et al.*, Central Insulin Action Activates Kupffer Cells by Suppressing Hepatic Vagal Activation via the Nicotinic Alpha 7 Acetylcholine Receptor. *Cell Rep* **14**, 2362-2374 (2016).
36. L. L. Hwang *et al.*, Sex differences in high-fat diet-induced obesity, metabolic alterations and learning, and synaptic plasticity deficits in mice. *Obesity (Silver Spring)* **18**, 463-469 (2010).
37. R. E. Stubbins, V. B. Holcomb, J. Hong, N. P. Nunez, Estrogen modulates abdominal adiposity and protects female mice from obesity and impaired glucose tolerance. *Eur J Nutr* **51**, 861-870 (2012).
38. U. S. Pettersson, T. B. Walden, P. O. Carlsson, L. Jansson, M. Phillipson, Female mice are protected against high-fat diet induced metabolic syndrome and increase the regulatory T cell population in adipose tissue. *PloS one* **7**, e46057 (2012).
39. H. Shi, D. J. Clegg, Sex differences in the regulation of body weight. *Physiol Behav* **97**, 199-204 (2009).
40. E. Kwon, T. Yoo, H. Y. Joung, Y. H. Jo, Hydrocarboxylic acid receptor 1 in BAT regulates glucose uptake in mice fed a high-fat diet. *PloS one* **15**, e0228320 (2020).
41. J. Nikkanen *et al.*, An evolutionary trade-off between host immunity and metabolism drives fatty liver in male mice. *Science* **378**, 290-295 (2022).
42. J. R. C. Nunes *et al.*, Thermoneutral housing does not accelerate metabolic dysfunction-associated fatty liver disease in male or female C57Bl/6J mice fed a Western diet. *American journal of physiology. Endocrinology and metabolism* **325**, E10-E20 (2023).
43. J. Zhang *et al.*, Effect of Chronic Western Diets on Non-Alcoholic Fatty Liver of Male Mice Modifying the PPAR-gamma Pathway via miR-27b-5p Regulation. *Int J Mol Sci* **22**, (2021).
44. A. Giordano *et al.*, White adipose tissue lacks significant vagal innervation and immunohistochemical evidence of parasympathetic innervation. *Am J Physiol Regul Integr Comp Physiol* **291**, R1243-1255 (2006).
45. T. J. Bartness, Y. B. Shrestha, C. H. Vaughan, G. J. Schwartz, C. K. Song, Sensory and sympathetic nervous system control of white adipose tissue lipolysis. *Mol Cell Endocrinol* **318**, 34-43 (2010).

46. G. Targher, K. E. Corey, C. D. Byrne, M. Roden, The complex link between NAFLD and type 2 diabetes mellitus - mechanisms and treatments. *Nat Rev Gastroenterol Hepatol* **18**, 599-612 (2021).
47. M. Harms, P. Seale, Brown and beige fat: development, function and therapeutic potential. *Nature medicine* **19**, 1252-1263 (2013).
48. M. Uldry *et al.*, Complementary action of the PGC-1 coactivators in mitochondrial biogenesis and brown fat differentiation. *Cell metabolism* **3**, 333-341 (2006).
49. M. J. Barbera *et al.*, Peroxisome proliferator-activated receptor alpha activates transcription of the brown fat uncoupling protein-1 gene. A link between regulation of the thermogenic and lipid oxidation pathways in the brown fat cell. *The Journal of biological chemistry* **276**, 1486-1493 (2001).
50. P. Seale *et al.*, Prdm16 determines the thermogenic program of subcutaneous white adipose tissue in mice. *The Journal of clinical investigation* **121**, 96-105 (2011).
51. M. P. Czech, Mechanisms of insulin resistance related to white, beige, and brown adipocytes. *Mol Metab* **34**, 27-42 (2020).
52. M. Alves-Bezerra, D. E. Cohen, Triglyceride Metabolism in the Liver. *Compr Physiol* **8**, 1-8 (2017).
53. A. Carino *et al.*, Gpbar1 agonism promotes a Pgc-1alpha-dependent browning of white adipose tissue and energy expenditure and reverses diet-induced steatohepatitis in mice. *Sci Rep* **7**, 13689 (2017).
54. A. Worthmann *et al.*, Cold-induced conversion of cholesterol to bile acids in mice shapes the gut microbiome and promotes adaptive thermogenesis. *Nature medicine* **23**, 839-849 (2017).
55. C. K. Lam *et al.*, Activation of N-methyl-D-aspartate (NMDA) receptors in the dorsal vagal complex lowers glucose production. *The Journal of biological chemistry* **285**, 21913-21921 (2010).
56. D. C. Kuo, G. C. Yang, D. S. Yamasaki, G. M. Krauthamer, A wide field electron microscopic analysis of the fiber constituents of the major splanchnic nerve in cat. *The Journal of comparative neurology* **210**, 49-58 (1982).
57. N. Jayaprakash *et al.*, Organ- and function-specific anatomical organization of vagal fibers supports fascicular vagus nerve stimulation. *Brain Stimul* **16**, 484-506 (2023).
58. M. Li *et al.*, Fatty acids promote fatty liver disease via the dysregulation of 3-mercaptopyruvate sulfurtransferase/hydrogen sulfide pathway. *Gut* **67**, 2169-2180 (2018).
59. E. Bruinstroop, E. Fliers, A. Kalsbeek, Restoring the autonomic balance to reduce liver steatosis. *The Journal of physiology* **597**, 4683-4684 (2019).
60. M. W. Bradbury, Lipid metabolism and liver inflammation. I. Hepatic fatty acid uptake: possible role in steatosis. *Am J Physiol Gastrointest Liver Physiol* **290**, G194-198 (2006).
61. A. Santoro, T. E. McGraw, B. B. Kahn, Insulin action in adipocytes, adipose remodeling, and systemic effects. *Cell metabolism* **33**, 748-757 (2021).
62. A. Carino *et al.*, BAR502, a dual FXR and GPBAR1 agonist, promotes browning of white adipose tissue and reverses liver steatosis and fibrosis. *Sci Rep* **7**, 42801 (2017).
63. A. Perino *et al.*, Central anorexigenic actions of bile acids are mediated by TGR5. *Nat Metab* **3**, 595-603 (2021).
64. A. Castellanos-Jankiewicz *et al.*, Hypothalamic bile acid-TGR5 signaling protects from obesity. *Cell metabolism* **33**, 1483-1492 e1410 (2021).
65. J. H. Jeong *et al.*, Cholinergic neurons in the dorsomedial hypothalamus regulate mouse brown adipose tissue metabolism. *Mol Metab* **4**, 483-492 (2015).
66. K. Matsumoto *et al.*, Advanced CUBIC tissue clearing for whole-organ cell profiling. *Nat Protoc* **14**, 3506-3537 (2019).

Acknowledgments

General: We thank Dr. Streamson Chua Jr. for their valuable feedback and comments on this study. We also thank Dr. Shun-Mei Liu and Licheng Wu for their technical assistance.

Funding: This work was supported by the NIH (R01 AT011653 and R03 TR003313 to Y.-H.J, R01 DK092246 to Y.-H.J and G.J.S., P30 DK020541 to Y.-H.J, G.J.S., and J.E.P. and DK110063 to J.E.P.).

Author contributions: J.Y.H performed viral injection, immunostaining, Western blotting, and ELISA assays, and analyzed data. J.O. and L.L. performed and analyzed spatial transcriptomics analysis. Y.-H.J designed the research, performed viral injection and immunocytochemistry, analyzed the data, and wrote the manuscript with inputs from G.J.S. and J.E.P. G.J.S and J.E.P. also designed the study.

Competing interests: The authors declare no conflict of interest.

Figure legends

Figure 1. Parasympathetic cholinergic system in the mouse liver

A. Images of confocal fluorescence microscopy showing co-expression of tdTomato and ChAT in a subset of DMV cholinergic neurons in ChAT^{Cre} mice receiving an injection of AAV.Php.eB-tdTomato into the liver, representing cholinergic neurons innervating the liver (white arrowheads).
Scale bar, 30 um

B. Images of confocal fluorescence microscopy showing the expression of vAChT-positive nerve terminals (green) in the parenchyma of the liver (inset: higher-magnification view of vAChT-positive terminals). Scale bar, 70 um

C. 3D projection view of confocal fluorescence microscopy image showing the expression of vAChT-positive nerve terminals (green, white arrowheads) in the cleared liver tissue (inset: image of cleared liver tissue). Blue: nucleus staining with DAPI. Scale bar, 20 um

D. Images of confocal fluorescence microscopy showing tdTomato-positive cholinergic neurons in the DMV (upper panel) and sypGFP-positive nerve terminals (bottom panel) in the liver of ChAT^{Cre} mice injected with AAV1-FLEX-tdTomato-T2A-sypGFP into the DMV. Hepatocytes and cholangiocytes received DMV cholinergic innervation (inset). Blue: nucleus staining with DAPI. Upper panel: scale bar, 30 um; lower panel: scale bar, 20 um

E. Z-stack image showing cholinergic nerve terminals (green) in the periportal area in cleared liver tissue collected from ChAT^{Cre} mice injected with AAV1-FLEX-tdTomato-T2A-sypGFP (upper panel). Bottom panel: 2D image of cholinergic nerve terminals shown in the upper panel. Scale bar: 50 um

F. 3D projection view of confocal fluorescence microscopy images showing co-expression of vAChT (red) - and GFP-positive nerve terminals (white arrowheads) in cleared liver tissue collected from ChAT^{Cre} mice injected with AAV1-FLEX-tdTomato-T2A-sypGFP. Scale bar, 20 um

G. Images of Western blot analysis of liver homogenates showing the expression of CHRM1-5, except for CHRM3.

H. Images of confocal fluorescence microscopy showing the expression of CHRM4 and vAChT in the liver parenchyma (upper panel). Scale bar, 25 um, Bottom panel: Higher magnification view of the white dotted square. CHRM4s were found adjacent to vAChT-positive nerve terminals (white arrows). Blue: nucleus staining with DAPI. Scale bar, 10 um

Figure 2. Deleting vagal cholinergic input to the liver reduces fat mass percentage during high-fat feeding.

A. Schematic illustration of the experimental configurations. AAVrg-FLEX-tdTomato (control, o) and AAVrg-FLEX-dTA viral vectors were injected directly into the livers of ChAT^{Cre} mice.

B. Images of confocal fluorescence microscopy showing reduced numbers of cholinergic neurons in the DMV of $ChAT^{Cre}$ mice receiving an injection of AAVrg-FLEX-dtA compared with the controls. Scale bar, 80 um cc: central canal, 12N: hypoglossal nucleus

C. Summary graph showing the number of cholinergic neurons on the left and right sides of the DMV in the control (n= 4 mice) and experimental mice (n= 4 mice). Unpaired *t*-test, **p<0.01

D. Images showing a lack of vAChT-positive nerve terminals in the liver parenchyma of $ChAT^{Cre + AAVrg-FLEX-dtA}$ mice (right panel). Left panel: control. Scale bar, 50 um

E and **F**. Summary plot showing a significant decrease in hepatic (control, n= 7 mice; experimental mice, n= 6 mice), but not plasma (control, n= 11 mice; experimental mice, n= 8 mice), ACh contents in $ChAT^{Cre + AAVrg-FLEX-dtA}$ mice compared to the controls. Unpaired *t*-test, *p<0.05

G. Graph showing changes in body weight of the control and experimental groups during high-fat diet feeding. There was a significant difference in body weight gain between the groups (control, n= 12 mice; experimental mice, n=21 mice; two-way ANOVA test, *p<0.05).

H. Graphs show a significant difference in body fat but not fat-free mass between the two groups (fat mass and lean mass, control, n= 9 mice; experimental mice, n=10 mice, unpaired *t*-test, *p<0.05).

I. Graphs showing that the experimental mice (n=7) exhibited a significantly lower ingWAT mass than the control group (n=8), whereas there was no difference in liver, interscapular WAT (isWAT), gonadal WAT (gWAT) and perigonadal WAT (pgWAT) mass between the groups. Unpaired *t*-test, *p<0.05

Figure 3. Deleting vagal cholinergic input to the liver prevents hepatic steatosis during high-fat diet feeding.

A and **B.** Macroscopic appearance of livers of $ChAT^{Cre}$ mice receiving AAVrg-FLEX-GFP and AAVrg-FLEX-dtA. E-Cad expression was lower in the control group than in the experimental group. Scale bar, 100 um

C and D. H & E staining of liver tissues revealed increased numbers of lipid droplets and ballooned hepatocytes in the controls compared to those in the experimental mice (top panel). Scale bar, 100 m. Bottom panel: Higher magnification view of liver tissue in the black dotted square. Scale bar, 30 m

E and F. Oil red O staining (red) of liver tissues from $ChAT^{Cre}$ mice with and without hepatic cholinergic input. The experimental group did not exhibit fat accumulation in the liver parenchyma during high fat feeding. Nuclear staining (blue): hematoxylin, Scale bar, 100 um

G. Graphs showing hepatic (n= 9 vs. 8 mice) and plasma (n= 11 vs. 12 mice) TG levels in the controls and experimental mice. There was a significant reduction in both hepatic and plasma TG levels in the experimental group relative to those in the control group (unpaired *t*-test, **p<0.01, ***p<0.001).

H. Summary graphs showing changes in hepatic mRNA expression of enzymes involved in lipid

metabolism. *Srebp1*c mRNA expression was significantly downregulated, while *Ppar*α mRNA expression was increased in the livers of ChAT^{Cre} mice receiving AAVrg-FLEX-dtA relative to controls (control, n= 8; experimental mice, n= 8, unpaired t-test, *p<0.05, **p<0.01).

Figure 4. Loss of hepatic cholinergic input induces beiging of ingWAT.

A. Representative images of the ingWAT of control and experimental mice.

B. Representative images of adipocytes in the ingWAT of control and experimental groups. Scale bar, 100 um

C and **D.** Plots showing the distribution of the average adipocyte size (left panel) . Right panel: The mean cell area was significantly smaller in the experimental groups than in controls (control, n=4 mice; experimental, n=5 mice, unpaired *t*-test, *p<0.05)

E. Summary graph showing changes in thermogenic gene expression in ingWAT of ChAT^{Cre} mice with and without DMV cholinergic neurons innervating the liver. Ablation of liver-projecting cholinergic neurons significantly upregulated the thermogenic gene expression (unpaired *t*-test, *p<0.05, **p<0.01) .

F and G. Western blot images of ingWAT showing an increase in UCP1 expression in experimental mice. Images of confocal fluorescence microscopy showing increased UCP1 expression in the ingWAT of experimental mice (**H**) . Scale bar, 50 um

H. Summary plots showing ingWAT temperature in the light and dark phases (control, n=5 mice; experimental, n= 4 mice, unpaired *t*-test, **p<0.01)

I. Western blot images showing a decrease in pS660-HSL expression in ingWAT of experimental mice relative to controls.

J. Summary plot showing plasma glycerol levels in the control (n= 8 mice) and experimental mice (n= 8 mice, unpaired *t*-test, *p<0.05)

Figure 5. Deleting liver-projecting cholinergic neurons elevates serum bile acid levels.

A. Graph showing mRNA expression of the enzymes involved in bile acid synthesis in liver. While there was no difference in *Cyp7a1* gene expression, the loss of hepatic cholinergic input significantly upregulated *Cyp7b1* mRNA expression (control (open circle), n=7-8 mice; experimental (closed black circle), n=7 mice).

B. Graphs showing *Cyp7a1* and *Cyp7b1* gene expression in the periportal (PP), midlobular (Mid), and pericentral (PC) zones in the livers of the controls and the experimental groups.

C. Graph showing fasting serum bile acid levels in the control (n=6 mice) and experimental groups (n=5 mice, unpaired t-test, *p<0.05).

D. Graph showing fasting serum bile acid profile in the control (n=4 mice) and experimental (n= 4 mice) mice. The Mann-Whitney test revealed a statistically significant difference between the two groups (*p<0.05).

Figure 6. Liver-ingWAT communication contributes to beiging of ingWAT via bile acids.

A. Graph showing mRNA and protein expression levels of *Tgr5* in ingWAT. There was a significant increase in TGR5 expression in the ingWAT of $ChAT^{Cre}$ mice that received AAVrg-FLEX-dtA (control (open circle), n=7 mice; experimental (closed circle), n=7 mice, unpaired *t*-test, **p<0.01).

B. Schematic illustration showing our experimental configurations.

C. Reduction in *Tgr5* gene and protein levels in $ChAT^{Cre}$ mice following administration of AAVrg-FLEX-dtA to the liver (black circle) and another injection of *Tgr5* siRNA into both sides of the ingWAT (blue circle) (unpaired *t*-test, *** P <0.001).

D. Graph showing changes in body weight during high-fat diet feeding. There was a significant increase in body weight in $ChAT^{Cre}$ mice that received AAVrg-FLEX-dtA into the liver and *Tgr5* siRNA to ingWAT (control, n= 8 mice; experimental mice, n= 14 mice, two-way ANOVA test, *p<0.05).

E. Graphs showing a significant difference in fat mass, but not fat-free mass, between the two groups (fat mass and lean mass, control, n= 12 mice; experimental mice, n=11 mice, unpaired *t*-test, *p<0.05).

F. Graphs showing that the experimental mice (n=5) exhibited a significantly lower tissue mass compared to that in the control group (n= 7 mice) (Unpaired *t*-test, **p<0.01; ***p<0.001)

G. Representative images of ingWAT sections stained with H&E. $ChAT^{Cre}$ mice without DMV cholinergic neurons innervating the liver receiving an injection of *Tgr5* siRNA into ingWAT exhibited larger adipocytes compared to the control mice (upper panel). Scale bar, 50 um Bottom panel: higher magnification view of the black dotted square. Arrow represents crown-like structure. Scale bar, 100 um

H and **I**. Plot showing the distribution of average adipocyte size. The mean cell area was significantly larger in the experimental group receiving *Tgr5* siRNA than in the experimental group receiving control siRNA (**I**) (control, n=5 mice; experimental, n=5 mice, unpaired *t*-test, *p<0.05)

Figure 7. *Tgr5* knockdown in ingWAT causes hepatic steatosis in $ChAT^{Cre}$ mice receiving AAVrg-FLEX-dtA during high-fat diet feeding.

A. Gel images showing the Western blot analysis of ingWAT from experimental mice revealed an increase in the expression of pS660-HSL when compared to the control group.

B. Graph showing plasma glycerol levels in the controls (black circle, n= 6 mice) and the experimental groups (blue circle, n= 5 mice). Unpaired *t*-test, **p<0.01

C and D. Representative images of liver sections stained with H&E (**C**) and Oil Red O (**D**). Upper panel: scale bar, 100 um;bottom panel: higher magnification view of the black dotted square scale bar, 50 um

E. Graph showing hepatic TG levels in the controls (n= 5 mice) and the experimental groups (n= 6 mice) . Unpaired *t*-test, *$p<0.05$

F. Schematic illustration of our proposed model. DMV cholinergic neurons sent direct axonal projections to the hepatocytes and cholangiocytes. The loss of parasympathetic cholinergic input to the liver results in elevated bile acid secretion, leading to TGR5 activation in ingWAT. This activation results in browning of ingWAT, reduced lipolysis, decreased plasma free fatty acids and glycerol. This inter-organ crosstalk is also critical in the development of systemic insulin resistance and hepatic steatosis in obese conditions. Hence, modulating the parasympathetic cholinergic innervation of the liver may offer a therapeutic avenue for restoring lipid metabolism in obesity and diabetes.

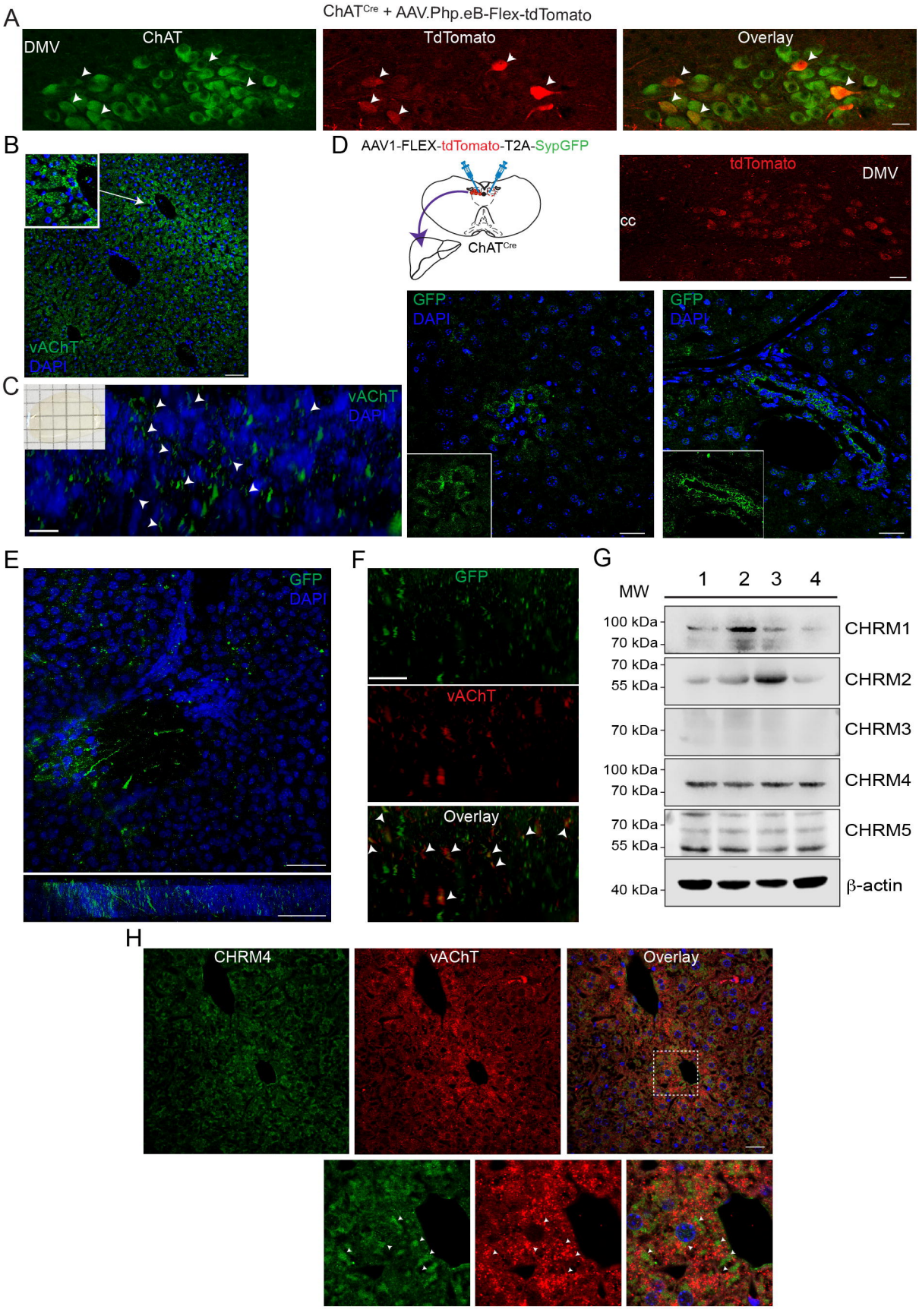
A
ChATCre + AAV.Php.eB-Flex-tdTomato
DMV
ChAT
TdTomato
Overlay
B
vAChT
DAPI
C
vAChT
DAPI
D
AAV1-FLEX-tdTomato-T2A-SypGFP
ChATCre
tdTomato
DMV
cc
GFP
DAPI
GFP
DAPI
E
GFP
DAPI
F
GFP
vAChT
Overlay
G
MW
1
2
3
4
100 kDa
70 kDa
CHRM1
70 kDa
55 kDa
CHRM2
70 kDa
CHRM3
100 kDa
70 kDa
CHRM4
70 kDa
55 kDa
CHRM5
40 kDa
β-actin
H
CHRM4
vAChT
Overlay

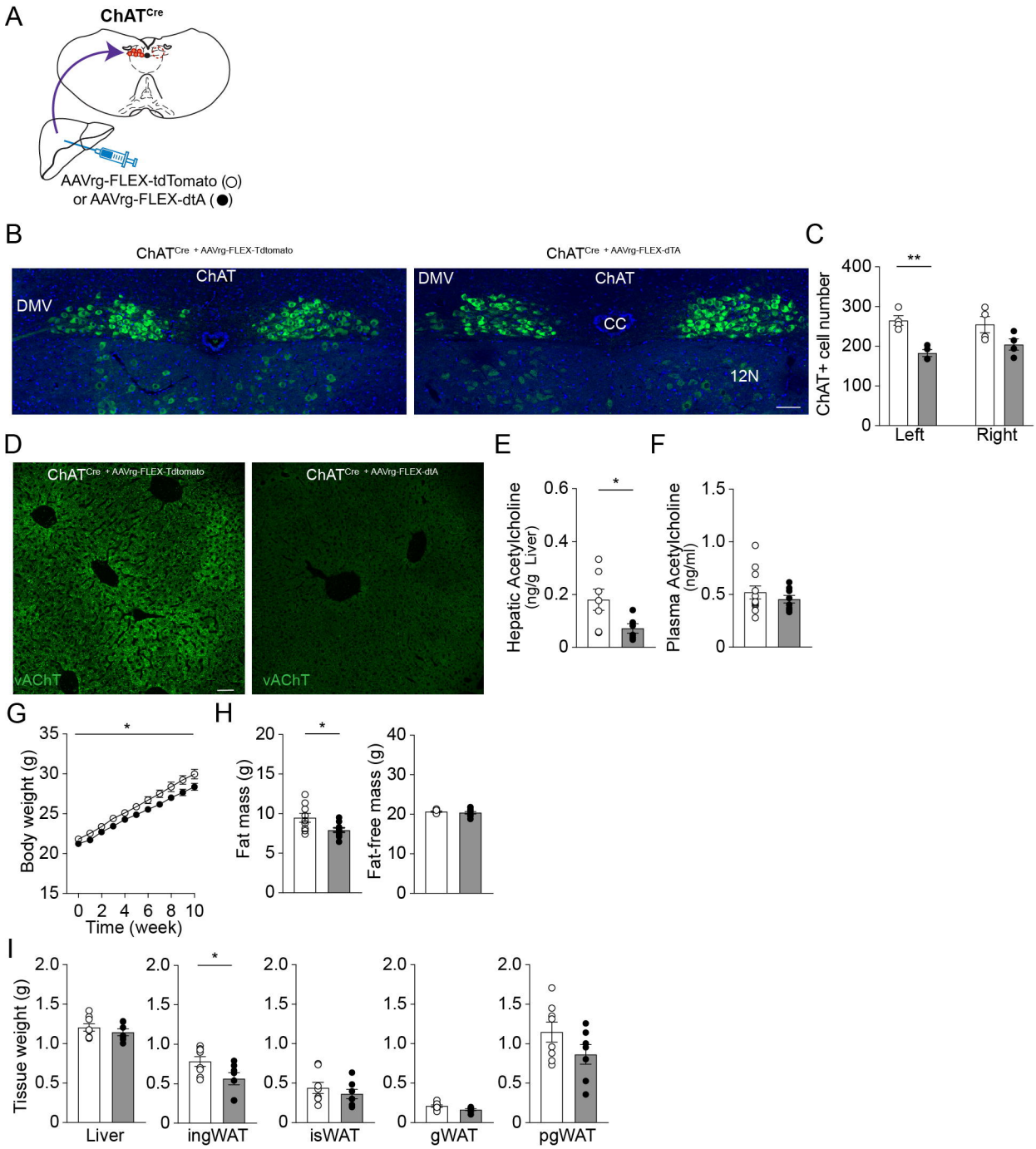
A
ChATCre
AAVrg-FLEX-tdTomato (○)
or AAVrg-FLEX-dtA (●)
B
ChATCre + AAVrg-FLEX-Tdtomato
ChATCre + AAVrg-FLEX-dTA
ChAT
DMV
CC
12N
C
ChAT+ cell number
Left
Right
D
ChATCre + AAVrg-FLEX-Tdtomato
ChATCre + AAVrg-FLEX-dtA
vAChT
E
Hepatic Acetylcholine (ng/g Liver)
F
Plasma Acetylcholine (ng/ml)
G
Body weight (g)
Time (week)
H
Fat mass (g)
Fat-free mass (g)
I
Tissue weight (g)
Liver
ingWAT
isWAT
gWAT
pgWAT

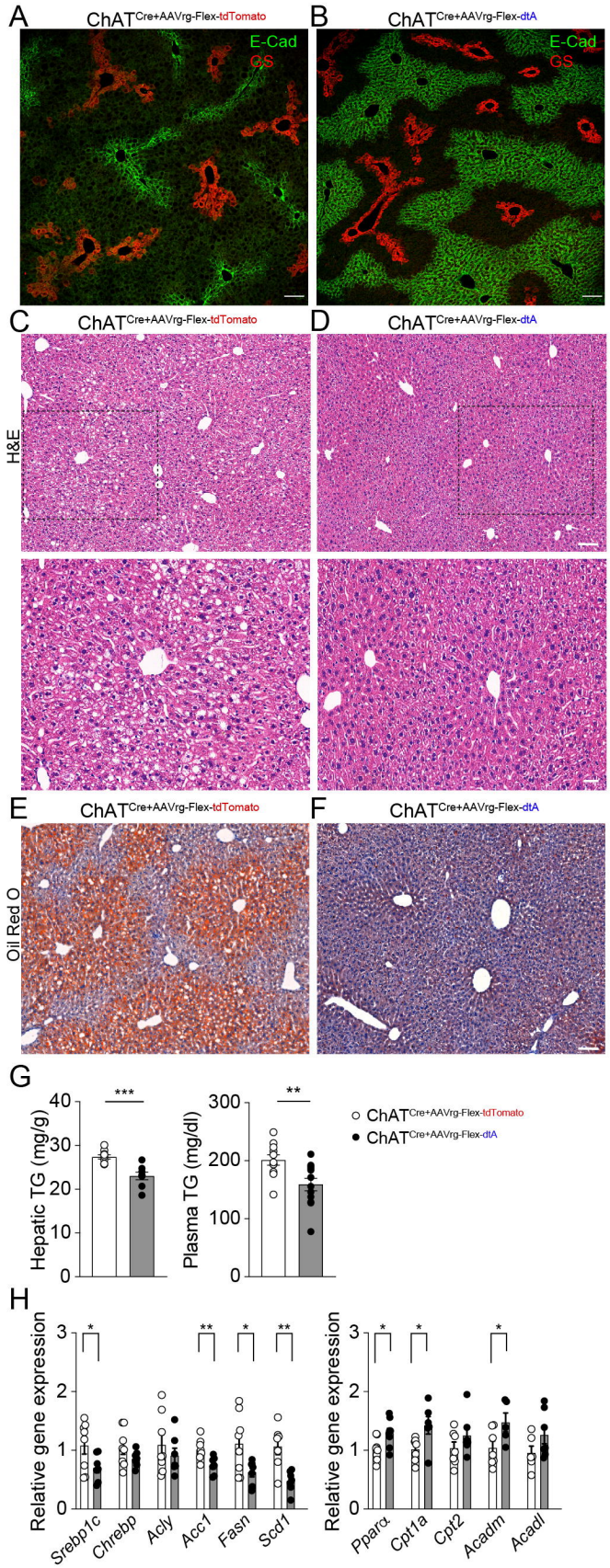
A
ChAT Cre+AAVrg-Flex-tdTomato
E-Cad
GS
B
ChAT Cre+AAVrg-Flex-dtA
E-Cad
GS
C
ChAT Cre+AAVrg-Flex-tdTomato
D
ChAT Cre+AAVrg-Flex-dtA
H&E
E
ChAT Cre+AAVrg-Flex-tdTomato
F
ChAT Cre+AAVrg-Flex-dtA
Oil Red O
G
Hepatic TG (mg/g)
Plasma TG (mg/dl)
***
**
ChAT Cre+AAVrg-Flex-tdTomato
ChAT Cre+AAVrg-Flex-dtA
H
Relative gene expression
Srebp1c
Chrebp
Acly
Acc1
Fasn
Scd1
Pparα
Cpt1a
Cpt2
Acadm
Acadl

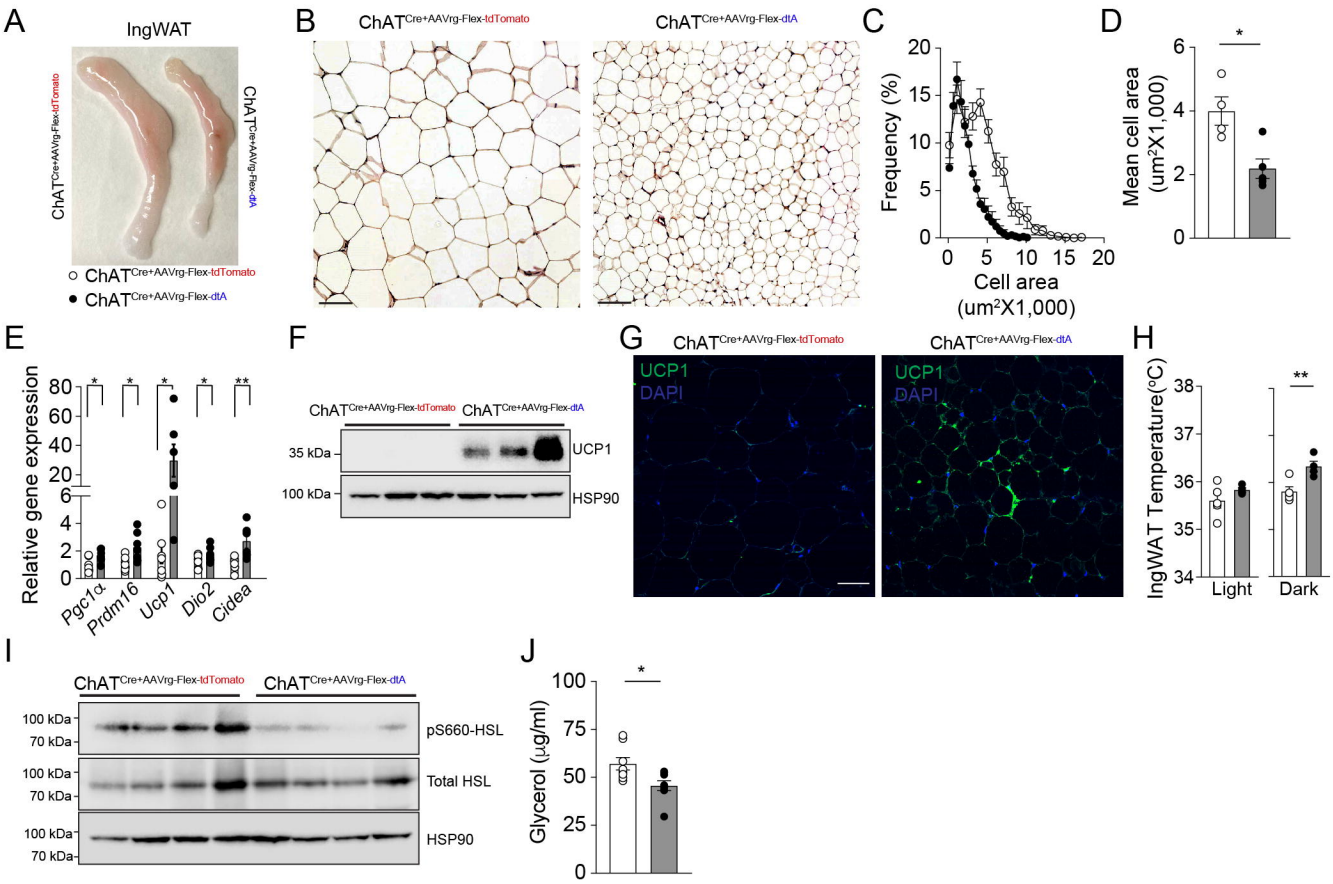
A
IngWAT
ChATCre+AAVrg-Flex-tdTomato
ChATCre+AAVrg-Flex-dtA
B
ChATCre+AAVrg-Flex-tdTomato
ChATCre+AAVrg-Flex-dtA
C
Frequency (%)
Cell area
(um2X1,000)
D
Mean cell area
(um2X1,000)
E
Relative gene expression
Pgc1α
Prdm16
Ucp1
Dio2
Cidea
F
35 kDa
100 kDa
UCP1
HSP90
G
UCP1
DAPI
H
IngWAT Temperature(°C)
Light
Dark
I
100 kDa
70 kDa
pS660-HSL
Total HSL
HSP90
J
Glycerol (μg/ml)

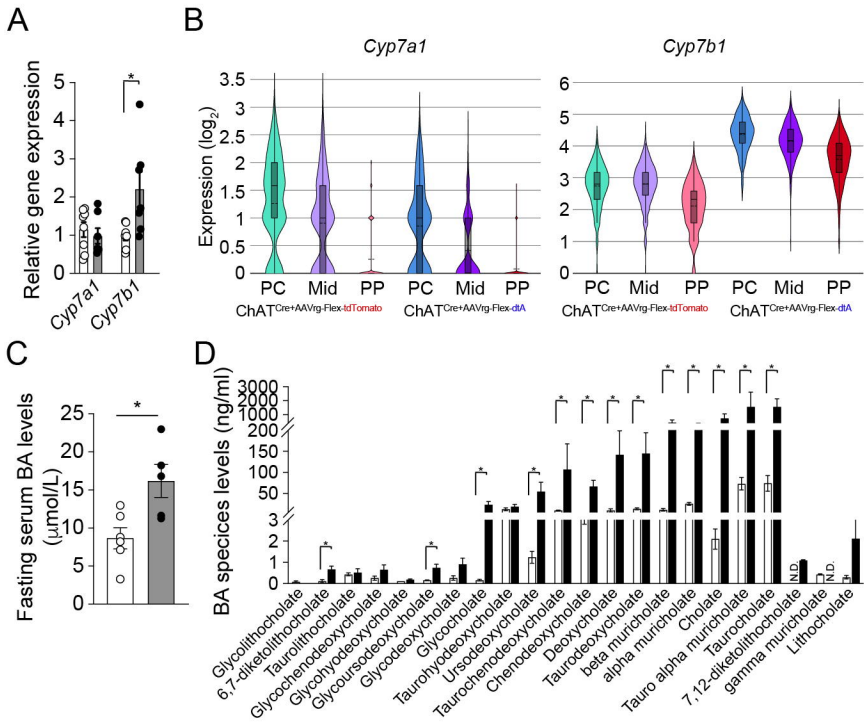
A
Relative gene expression
Cyp7a1
Cyp7b1
B
Cyp7a1
Cyp7b1
Expression (log2)
PC
Mid
PP
ChATCre+AAVrg-Flex-tdTomato
ChATCre+AAVrg-Flex-dtA
C
Fasting serum BA levels (μmol/L)
D
BA specices levels (ng/ml)
Glycolithocholate
6,7-diketolithocholate
Taurolithocholate
Glycochenodeoxycholate
Glycohyodeoxycholate
Glycoursodeoxycholate
Glycodeoxycholate
Glycocholate
Taurohyodeoxycholate
Ursodeoxycholate
Taurochenodeoxycholate
Chenodeoxycholate
Deoxycholate
Taurodeoxycholate
beta muricholate
alpha muricholate
Cholate
Tauro alpha muricholate
Taurocholate
7,12-diketolithocholate
gamma muricholate
Lithocholate
N.D.

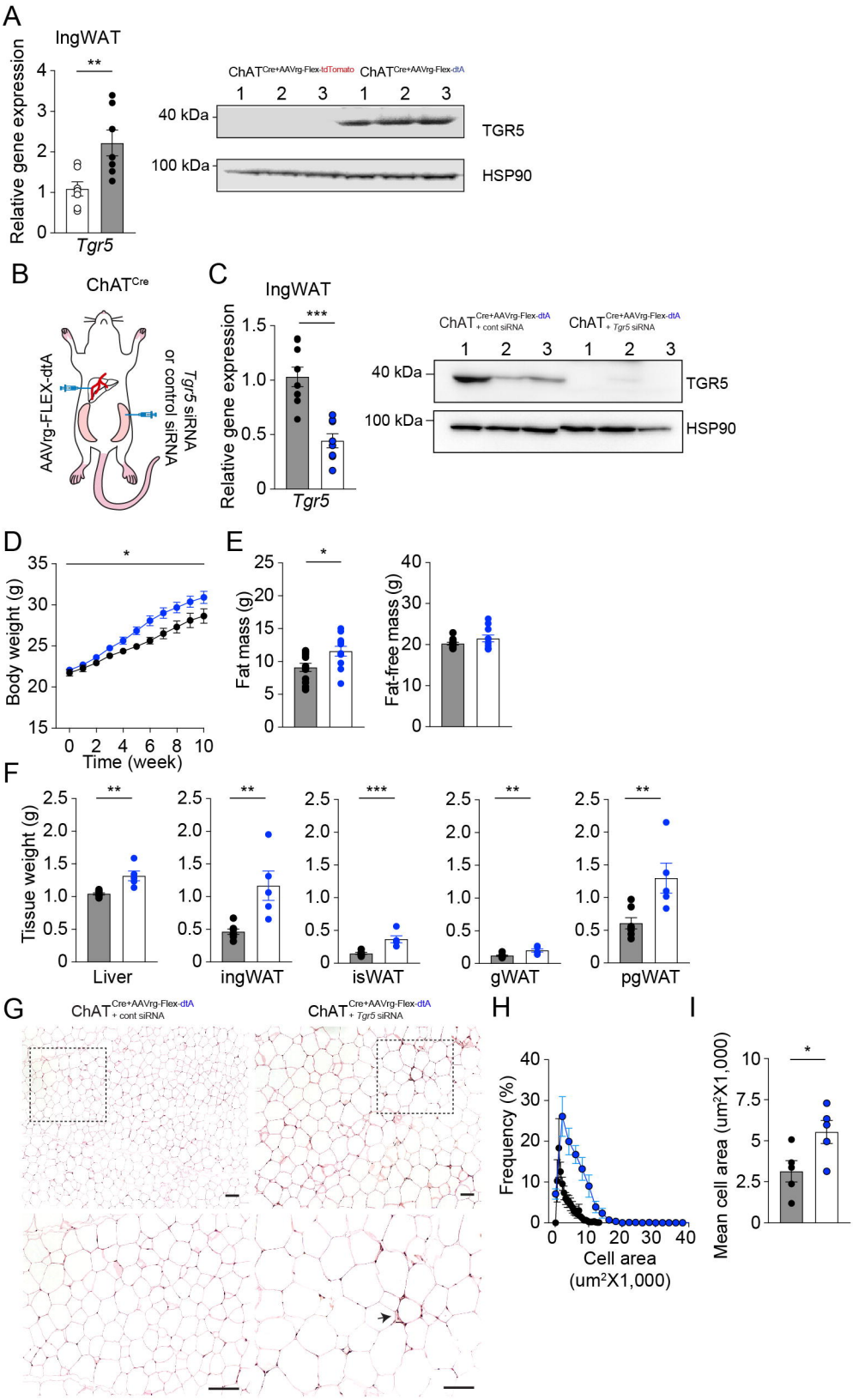
A
IngWAT
Relative gene expression
**
Tgr5
ChATCre+AAVrg-Flex-tdTomato
ChATCre+AAVrg-Flex-dtA
1 2 3 1 2 3
40 kDa
100 kDa
TGR5
HSP90
B
ChATCre
AAVrg-FLEX-dtA
Tgr5 siRNA
or control siRNA
C
IngWAT
***
Relative gene expression
Tgr5
ChATCre+AAVrg-Flex-dtA + cont siRNA
ChATCre+AAVrg-Flex-dtA + Tgr5 siRNA
1 2 3 1 2 3
40 kDa
100 kDa
TGR5
HSP90
D
*
Body weight (g)
Time (week)
E
*
Fat mass (g)
Fat-free mass (g)
F
Tissue weight (g)
Liver
ingWAT
isWAT
gWAT
pgWAT
G
ChATCre+AAVrg-Flex-dtA + cont siRNA
ChATCre+AAVrg-Flex-dtA + Tgr5 siRNA
H
Frequency (%)
Cell area
(um2X1,000)
I
*
Mean cell area (um2X1,000)

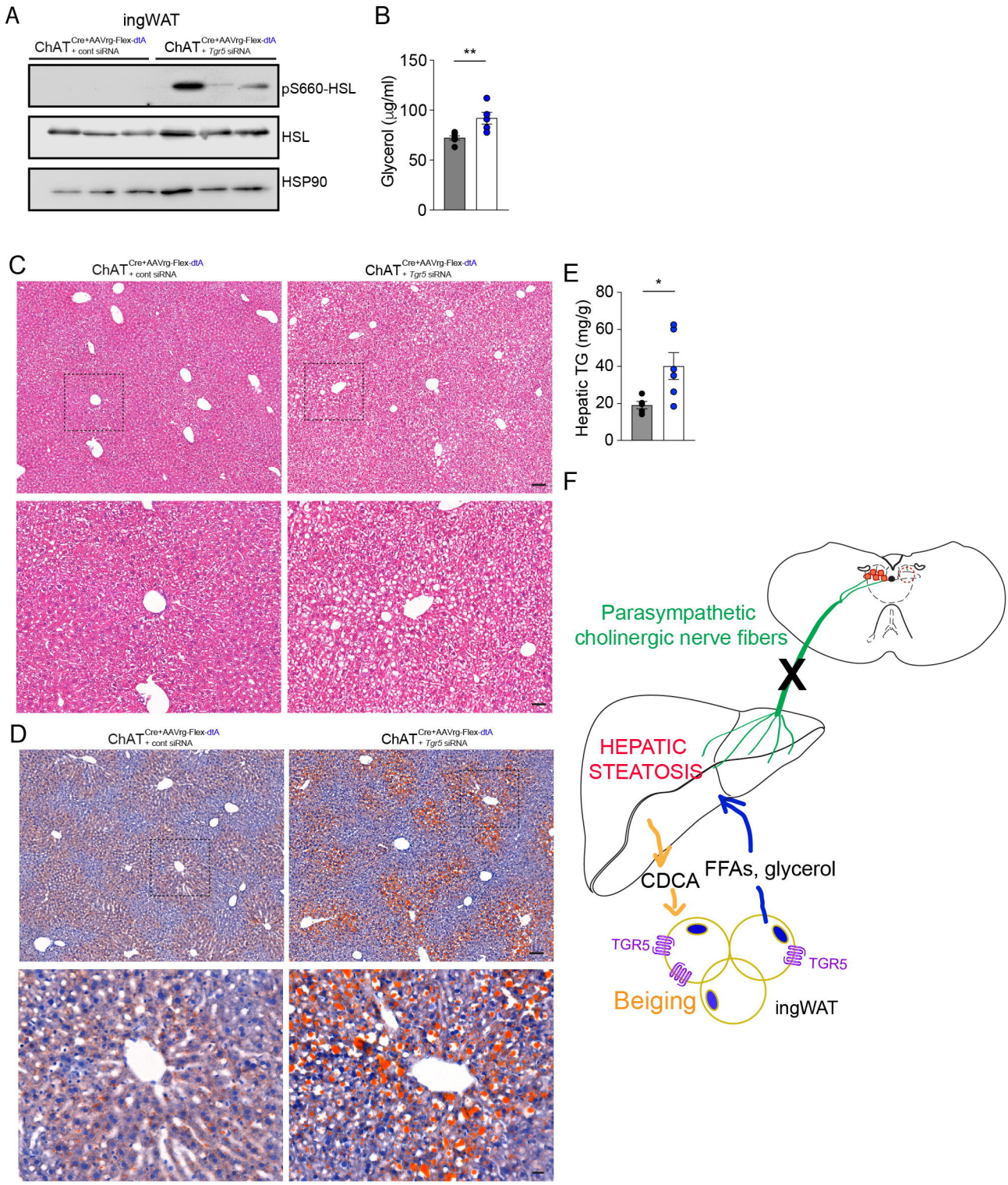
A
ingWAT
ChAT Cre+AAVrg-Flex-dtA + cont siRNA
ChAT Cre+AAVrg-Flex-dtA + Tgr5 siRNA
pS660-HSL
HSL
HSP90
B
Glycerol (μg/ml)
150
100
50
0
**
C
ChAT Cre+AAVrg-Flex-dtA + cont siRNA
ChAT Cre+AAVrg-Flex-dtA + Tgr5 siRNA
D
ChAT Cre+AAVrg-Flex-dtA + cont siRNA
ChAT Cre+AAVrg-Flex-dtA + Tgr5 siRNA
E
Hepatic TG (mg/g)
80
60
40
20
0
*
F
Parasympathetic cholinergic nerve fibers
X
HEPATIC STEATOSIS
CDCA
FFAs, glycerol
TGR5
TGR5
Beiging
ingWAT